CM² MAGAZINE

第 56 期

南方科技大学海洋磁学中心

https://cm2.sustech.edu.cn/

创刊词

海洋是生命的摇篮，是文明的纽带。地球上最早的生命诞生于海洋，海洋里的生命最终进化成了人类，人类的文化融合又通过海洋得以实现。人因海而兴。

人类对海洋的探索从未停止。从远古时代美丽的神话传说，到麦哲伦的全球航行，再到现代对大洋的科学钻探计划，海洋逐渐从人类敬畏崇拜幻想的精神寄托演变成可以开发利用与科学研究的客观存在。其中，上个世纪与太空探索同步发展的大洋科学钻探计划将人类对海洋的认知推向了崭新的纬度：深海（deep sea）与深时（deep time）。大洋钻探计划让人类知道，奔流不息的大海之下，埋藏的却是亿万年的地球历史。它们记录了地球板块的运动，从而使板块构造学说得到证实；它们记录了地球环境的演变，从而让古海洋学方兴未艾。

在探索海洋的悠久历史中，从大航海时代的导航，到大洋钻探计划中不可或缺的磁性地层学，磁学发挥了不可替代的作用。这不是偶然，因为从微观到宏观，磁性是最基本的物理属性之一，可以说，万物皆有磁性。基于课题组的学科背景和对海洋的理解，我们对海洋的探索以磁学为主要手段，海洋磁学中心因此而生。

海洋磁学中心，简称 CM^2，一为其全名“Centre for Marine Magnetism”的缩写，另者恰与爱因斯坦著名的质能方程 $E = MC^2$ 对称，借以表达我们对科学巨匠的敬仰和对科学的不懈追求。

然而科学从来不是单打独斗的产物。我们以磁学为研究海洋的主攻利器，但绝不仅限于磁学。凡与磁学相关的领域均是我们关注的重点。为了跟踪反映国内外地球科学特别是与磁学有关的地球科学领域的最新研究进展，海洋磁学中心特地主办 CM^2 Magazine，以期与各位地球科学工作者相互交流学习、合作共进！

“海洋孕育了生命，联通了世界，促进了发展”。 21 世纪是海洋科学的时代，由陆向海，让我们携手迈进中国海洋科学的黄金时代！

目 录

岩石磁学演绎

第 46 章 磁学参数的多解性总结

如前所述，磁学参数已广泛用于解决环境问题。Dekkers [1997] 提出了磁学参数存在的一些弊端（例如，一些参数的非单一性，磁性矿物混合体的复杂性）。但是，在环境过程中通常忽略了磁学参数解释的非单一性。所以将磁学参数与自然过程联系起来时需要仔细考虑这些多解性。

1. 单一磁性矿物磁学参数的内在复杂性

即使磁学性质只由一种磁性矿物控制，还是会受多种因素影响，包括磁畴状态、测量频率、磁相互作用、杂质等。下面会逐一介绍这些变量的影响。

1.1 磁畴状态

正如前面提到的，矿物的磁学性质会随着磁畴状态系统变化。尽管 SP 和 MD 颗粒的磁学行为存在本质的不同，但是它们的许多磁学性质十分相似。例如，SP 和 MD 颗粒的磁化率值远高于 SD 和细粒 PSD 颗粒的磁化率。如果样品中磁性矿物含量是固定的，那么χ的增强主要是由于 SP 颗粒增多（例如，成土作用形成的中国黄土古土壤）或者颗粒变粗形成更多粗 PSD 或 MD 颗粒（如受风动力控制的西伯利亚古土壤）。对于这个问题的解决办法是测出磁性矿物混合的粒径分布。如果颗粒存在相对较宽的粒径分布，包括 SP 和 SD 颗粒，那么χfd%可用来检测 SP/SD 界限（磁铁矿：~20-25 nm）附近的粘滞 SP 颗粒。χfd 和全样χ的正相关关系表明 主要由细颗粒含量控制，而不是粒径的变化。然而，χfd (或者χfd%)对极细的颗粒（<10 nm）并不敏感，因为这些 SP 颗粒的χ不随测量频率变化，低温（<300K）χfd 实验可以解决这个问题[Worm and Jackson, 1999; Liu et al., 2005a; Jackson et al., 2006; Egli, 2009]。然而，这些复杂的岩石磁学实验并没有被广泛普及。在这种情况下，结合χfd, χ/Ms，ARM 和χ的相关性，以及 IRM 随时间的粘滞衰减可以检测 SP 颗粒的存在。

对于较粗的 PSD 和 MD 磁铁矿或者钛磁铁矿，由于磁畴壁的松弛，χfd 在 50 K 左右达到一个峰值[Šimša et al., 1985; Radhakrishnamurthy and Likhite, 1993; Moskowitz et al., 1998; Skumryev et al., 1999; Kosterov, 2003; Lagroix et al., 2004]，这很容易与几纳米的 SP 颗粒信息混淆。Liu et al. [2010] 在阿根廷土壤样品中观

测到了这个峰值，CBD 处理可以溶解成土作用形成的细粒亚铁磁性矿物，但是这个峰值并不受 CBD 处理的影响。这就说明阿根廷土壤在该处的峰值不是由超细 SP 颗粒引起的，而是由粗粒的成岩矿物引起的，因此排除了这种成土颗粒的特殊形成机制。

ARM 也会受到磁畴状态影响。根据定义，SP 颗粒不能携带剩磁，但是天然样品通常存在一个粒径分布（例如对数正态分布），所以 ARM 与平均粒径之间不存在一致变化。单位质量的 SD 颗粒具有最高的 ARM，所以 ARM 用于指示 SD 颗粒的含量。然而，当 PSD/MD 颗粒的含量很高时，它们对全样 ARM 的贡献是不容忽视的。在这种情况下，可先对 ARM 进行 20 mT 交变退，去除 PSD/MD 颗粒的影响。通常，在半定量测量 SD 颗粒含量方面，部分 ARM（pARM）（经过 20 mT 交变退的 ARM）要优于 ARM [Liu et al., 2005d]。

除了与含量有关的磁学参数，两个参数的比值可排除磁性矿物含量的影响，将与粒径有关的信息增强。最常用的比值有 ARM/χ、ARM/SIRM、χ/Ms、Mrs/Ms 和 χfd/χ 。这些比值的多解性主要有两个原因：首先，该比值继承了单一参数（如χ和 ARM）的内在多解性。另外，比值受分母控制。双变量相关图可解除这种影响，鉴别出磁颗粒粒径变化信息。例如，χ_{ARM} 和χ的线性相关关系表明对两参数有贡献的磁颗粒的粒径分布是稳定的。相反，χ_{ARM} /χ 的变化指示了磁性矿物粒径的变化。

同样地，粒径分布对χ_{fd}/χ (或者χ_{fd}%)的影响明显高于磁性矿物含量的影响[Worm, 1998]。例如，中国黄土/古土壤中成土作用形成的亚铁磁性纳米颗粒具有固定的粒径分布，峰值粒径为 20-25 nm，这与磁赤铁矿的 SP/SD 界限一致[Liu et al., 2004c, 2005a, 2007a]。穿过黄土-古土壤界限时χ_{fd} 和χ的线性相关关系证明了这一点，然而在初始土壤中χ_{fd}%会随着成土作用增强而增加。所以，假设χ_{fd}%只受粒径分布变化影响会得到错误的结论，即越成熟的土壤，其成土作用形成的磁赤铁矿的粒径分布越窄，这种明显矛盾的结果主要是由于忽略了成岩作用的影响[Liu et al., 2004c]。

1.2 同形替代

磁性矿物中的 Fe 通常存在同形替代（在晶体结构中被 Ti 或者 Al 替代）。实际情况中人们通常把钛磁铁矿作为一种新的矿物而不是 Ti 替代磁铁矿，所以磁

铁矿和钛磁铁矿之间的混淆就可以解决了。然而，离子替代的赤铁矿和针铁矿的性质仍然存在不确定性。它们属于高矫顽力矿物，但是事实上它们具有较宽的矫顽力分布[e.g., Roberts et al., 2006]。化学计量的针铁矿矫顽力高于几十特斯拉[Rochette et al., 2005]，但是，由于它的 T_N 较低（~120° C），T_N 随着 Al 含量的增加迅速降低，矫顽力也相应的降低，所以当 T_N 达到室温时，铝替代针铁矿便是顺磁性的，那么矫顽力应该是零。Liu et al. [2007b] 提出当铝替代针铁矿中的铝含量大于 13-15 mol%（土壤中含铝针铁矿的合理值）时，其在室温下的矫顽力小于 100 mT，这和磁铁矿矫顽力相当。赤铁矿与铝替代也存在复杂的对应关系，赤铁矿的 T_N 是 680 ºC，所以铝替代对 T_N 的影响不是很重要。但是，铝替代对赤铁矿矫顽力的影响主要通过两种方式，改变其内部应力和晶胞大小。初始铝替代会增加含铝赤铁矿的内部应力，进而增加其矫顽力，但是，随着铝替代的增加，晶胞减小，含铝赤铁矿粒径减小，最终会降低其矫顽力。当粒径减小到 20-30 nm 之下，即纯赤铁矿的 SP/SD 界限[Banerjee, 1971]时，含铝赤铁矿的矫顽力接近于零（i.e.，含铝赤铁矿变成了 SP 颗粒）。

含铝赤铁矿较宽的矫顽力分布严重影响了其他参数，如 HIRM 和 S-ratio，这两个参数分别用于追踪赤铁矿和针铁矿的绝对含量和相对含量。显然，这两个参数不能用来测量纯针铁矿（矫顽力极高）或者铝含量高于 13-15 mol%（矫顽力低于 100 mT）的含铝针铁矿。而含铝赤铁矿和针铁矿的 HIRM 与全样的矫顽力呈正相关，所以这两个参数只有在“硬度”参数（L-ratio）稳定时才能正常应用。

1.3 磁相互作用

在环境磁学研究中，通常假设磁性颗粒之间的磁相互作用对磁学参数的影响可以忽略。但是，磁相互作用对 SP/SD 处颗粒的磁学性质具有十分重要的影响，Sugiura [1979] 提出 ARM/SIRM 随着磁铁矿含量的增加而减小，Yamazaki and Ioka [1997a]对太平洋沉积物的研究发现 ARM/χ与沉积物中磁性矿物的含量相关。这表明磁相互作用对 ARM/χ的影响使该参数作为粒径指标的解释更为准确，另外也可以将 ARM 作为一个可靠的磁性矿物含量指标来估测相对地磁古强度[Yamazaki, 2008]。

根据数值模拟的结果，Muxworthy et al. [2004] 提出相互作用的 SD 颗粒会表现出 MD 颗粒的行为，这说明相互作用的 SD 颗粒比无相互作用的颗粒更软。

相反，SP 颗粒之间的相互作用会使它们的磁各向异性增强，表现出 SD 颗粒的行为，导致χ_{fd}的突然降低[Muxworthy, 2001]。同样的，粒径大于 100 nm 的 PSD 磁铁矿在相互作用的影响下磁性更稳定，例如，其磁滞参数会由 PSD 向 SD 区域移动[Muxworthy, 2003]。

三个主要方法可用来检测磁相互作用的影响：1）测量 Cisowski [1981]中的 Wohlfarth R 值；2）测量 FORC 图中平行于 Y 轴的相互作用场分布[Pike et al., 1999; Roberts et al., 2000; Muxworthy et al., 2004]；3）确定 ARM/χ (或者 ARM/SIRM)与磁性矿物含量的相关性[Yamazaki and Ioka, 1997a; Yamazaki, 2008]。无相互作用的 SD 颗粒 R=0.5，磁相互作用会使 R 值降低[Cisowski, 1981]。但是，对于 R<0.5 的理解还存在不确定性，因为无相互作用的 SD 颗粒也可能得到该范围的值。另外，相互作用的影响可以根据 FORC 图在 Y 轴较宽的展布判断。例如，天然样品中强相互作用的胶黄铁矿就属于这种类型[Roberts et al., 2006]。Pike et al. [1999] 提出，与 Cisowski [1981] 的方法相比，FORC 图对磁相互作用的检测更为灵敏。最后，ARM/χ与磁性矿物含量之间的反相关关系可用来检测相互作用[Yamazaki and Ioka, 1997a; Yamazaki, 2008]。但是，利用该参数的北太平洋沉积物是多种磁性矿物的混合，磁相互作用组分是否与沉积物中的强磁性组分一致还不明确。尽管在利用这些方法研究相互作用时要留意，但是它们都可以用来检测磁相互作用，并且 FORC 图是测量磁相互作用最为有效的方法[Pike et al., 1999]。

2 与环境过程相关的不确定性分析

利用各种复杂的磁学测量和数据分析方法可以解决磁学参数解释的不确定性。对于多种矿物混合，分离磁信息是十分重要的。但是，磁学参数和环境过程之间的联系还存在一些障碍，不像气候指标与环境过程之间存在定量关系（如氧同位素），在两个相反的气候状态相互转换过程，磁学参数通常只能提供半定量信息。大部分情况下，磁学性质通过大量的环境过程来与气候关联。从源区到沉积，岩石风化析出的磁性矿物经历了构造、环境和气候过程，这些过程搬运并改变了这些矿物。例如，中国黄土中的 PSD/MD 磁铁矿的粒径变化与源区距离或者风强度有关，或者与二者都有关，鉴别这两个过程的影响需要更详细的信息。另外，天然样品中的磁性矿物是多物源的。例如，人们最初认为北太平洋 ODP882

孔海洋沉积物的χ信息代表了 IRD 的信息[Haug et al., 1995]，但是，近来的研究发现χ的变化主要是粉尘和火山灰输入引起的[Bailey et al., 2011]。其次，沉积后改造过程也会不同程度的改变磁性矿物，进而掩盖了初始的环境信息。

所以，在解释岩石磁学结果时需要考虑源区和沉积物之间的可能联系。如果只是对全样进行实验的话，很多过程可能会使结果变得不可信[Oldfield et al., 2009]，如水动力分选、搬运过程中的分选、沉积后改造、成土作用以及生物成因磁性矿物的贡献。尽管在解决这些不确定性时需要留心，但是上面总结的方法还是可以帮助我们得到比较有力的结论。

文献速递

1. 大陆边缘地区沉积物埋藏有机碳丰度、来源及年龄的控制机制

翻译人：仲义 zhongy@sustech.edu.cn

Blanca, A. Elena, R. Negar, H., et al. ***Controls on the abundance, provenance and age of organic carbon buried in continental margin sediments*** *[J]* ***Earth and Planetary Science Letters****, 2021, 558, 116759.*

https://doi.org/10.1016/j.epsl.2021.116759

摘要：大陆边缘作为有机生物主要的海洋栖息地，在碳循环过程中发挥着重要碳埋藏作用。然而，对于这些非均质、动态变化的有机质分布和保存的控制因素，我们的认识仍然存在差距。特别是水动力过程对沉积有机碳的年龄、丰度和稳定同位素变化的影响还存在争议。本文中作者描述了来自 7 个大陆边缘地区的沉积物全岩和不同粒级的有机碳结果。结果显示了水动力颗粒分选过程会对有机碳的放射性年龄具有一定的影响。矿物颗粒的水动力特征及其与有机质相互作用的性质均对有机质含量有影响，而两者对有机质含量的 $\delta^{13}C$ 没有产生作用。因为有机碳优先保存在细粉砂（2-8 μm）组分，这部分占据了全岩沉积物很大部分。相对于黏土或者粗粉砂组分，远源的细粉砂迁移和再沉积的过程可能会直接改变当地有机碳的特征。因此作者认为不同粒级的有机碳年龄和含量之间的差异大小由水动力分选和其他特定地点过程的相互作用决定，可以分为三种不同类型的沉积环境：萌芽期、稳定期和成熟期。每个区域都具有不同程度上的垂直和横向有机碳供应，反映了当地生物生产力和上覆地表水碳出口以及驱动水动力过程的物理作用力。这个机制框架可进一步完善有机碳埋藏的评价，并限制大陆边缘沉积层序中同时期替代性信号可能产生的混叠程度。

ABSTRACT: Continental margins play a fundamental role in the carbon cycle as primary oceanic locations of organic carbon (OC) burial. However, gaps remain in our understanding of factors controlling the distribution and preservation of organic matter (OM) in these heterogeneous and dynamic systems. In particular, the impact of hydrodynamic processes on the age, abundance, and stable isotopic composition of sedimentary OC is poorly constrained. Here, we characterize the OC present in bulk and grain-size sediment fractions from seven continental margin settings. Our results reveal that hydrodynamic particle sorting processes exert a ubiquitous influence on the radiocarbon

age of OC. Both, hydrodynamic characteristics of mineral particles and the nature of their interactions with OM influence sedimentary OC content, whereas no significant influence of either effect is manifested in corresponding δ13C values. Since OC preferentially resides within the fine silt fraction (2-8 μm), and this fraction accounts for a substantial fraction of the bulk sediment mass, translocation and subsequent re-deposition of distant fine silt has the greatest potential to distort local OC signatures relative to those associated with clay or coarse silt fractions. We suggest that the magnitude of differences in 14C-age and OC content among grain-size fractions, determined by the interplay of hydrodynamic sorting and other site-specific processes, allow three different categories of depositional environment to be defined: initial, stable, and mature. Each domain is characterized by different degrees of vertical and lateral OC supply that reflect influences of local biological productivity and carbon export from overlying surface waters and physical forcing that drive hydrodynamic processes. This generic framework may serve as a guide to refine assessment of OC burial and to constrain the magnitude of potential aliasing among co-eval proxy signals in continental marginsedimentary sequences.

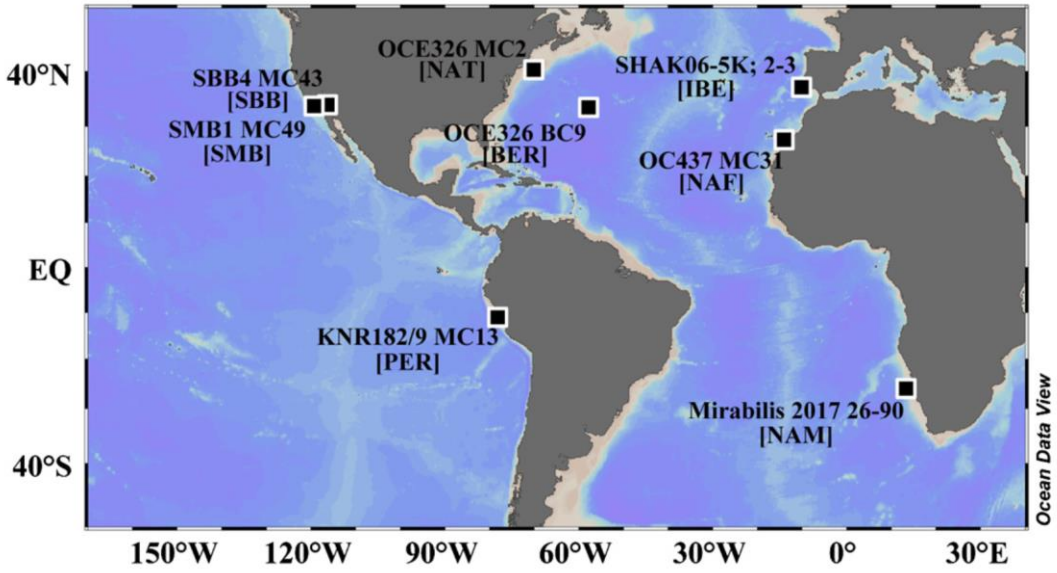

Figure 1. Locations of the surface sediment samples analyzed in this study and sample SHAK06-5K; 2-3 cm from Magill et al. (2018). The corresponding acronym for each site is shown within brackets

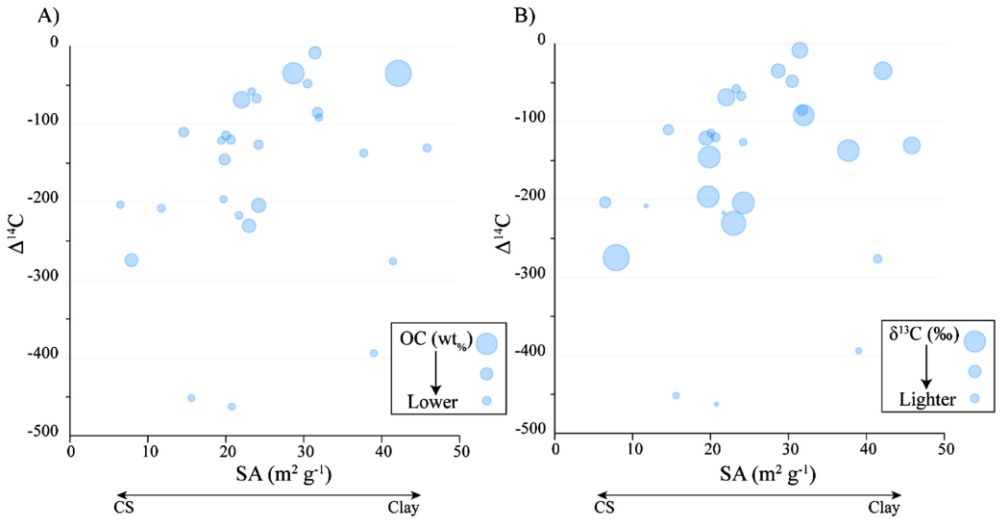

Figure 2. Relationship between 14C and SA with OC content (A) and δ13COC (B).

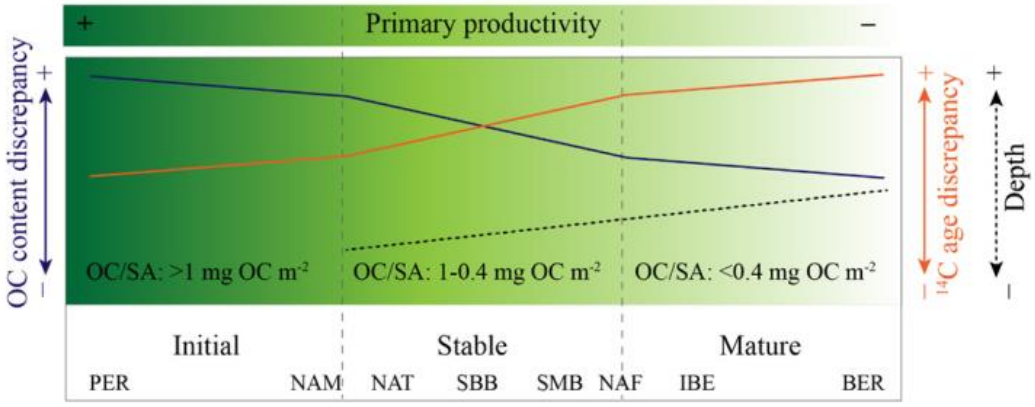

Figure 3. Conceptual model summarizing the characteristics of the “Initial”, “Stable”, and “Mature” systems as explained in section 4

2. 镁同位素揭示南海次海盆尺度的地幔不均一性

翻译人：冯婉仪 fengwy@sustech.edu.cn

Zhong Y, Zhang G L, Jin Q Z, et al. ***Sub-basin scale inhomogeneity of mantle in the South China Sea revealed by magnesium isotopes*** *[J]. Science Bulletin, 2021, in press.*

https://doi.org/10.1016/j.scib.2020.12.016

摘要：南海是西太平洋最大的伸展盆地，它形成于欧亚大陆边缘的裂谷作用之后。由于缺乏海底火成岩地壳的样品，其下伏地幔的性质仍然是个谜。国际海洋发现计划 349 航次对南海西南次海盆（U1433 站位）和东部次海盆（U1431 站位）的海底玄武岩进行了取样。获取的玄武岩样品具有不同的源岩岩性和地球化学特征。我们对这些站位的海底玄武岩的镁同位素组成进行研究，以阐明这种大规模地幔不均匀性的成因。结果表明 U1431 站位的玄武岩具有类似地幔的 δ^{26}Mg 值，其平均 δ^{26}Mg 值为-0.27‰ ± 0.06‰（2SD; n = 10）。连同不均一的 Sr-Nd-Pb-Hf 同位素组成，U1433 站位玄武岩平均 δ^{26}Mg 值（-0.20‰ ± 0.06‰; 2SD;n = 8）高于 U1431 站位玄武岩和正常地幔的平均 δ^{26}Mg 值。其较重的 Mg 同位素组成和较低的 ^{206}Pb/^{204}Pb 比值（~17.7）表明，U1433 站位玄武岩受洋脊之下地幔中拆沉的大陆弧岩石圈的重熔作用影响。Mg 同位素与 Sr-Nd 同位素的耦合证明了 U1431 站位玄武岩的 δ^{26}Mg 值是由拆沉的大陆弧岩石圈与附近海南地幔柱的混合作用所形成的，其中，拆沉的大陆弧岩石圈与附近海南地幔柱的 δ^{26}Mg 值分别高于正常地幔值和低于正常地幔值。从 Mg 同位素角度看，西南次海盆和东部次海盆地幔成分不均一，并且它们的地幔演化历史明显不同。

ABSTRACT: The South China Sea (SCS) is the largest extensional basin in the western Pacific and was formed after rifting of the Euro–Asian continental margin. The nature of its underlying mantle remains enigmatic due to the lack of sampling of the seafloor's igneous crust. The International Ocean Discovery Program Expedition 349 cored seafloor basalts of the southwestern (Site U1433) and eastern (Site U1431) SCS sub-basins. The recovered basalt samples exhibit different source lithologies and geochemistries. The Mg isotopic compositions of seafloor basalts from these sites were investigated to elucidate the origin of this large-scale mantle inhomogeneity. Results indicate that the Site U1431 basalts have a mantle like average δ26Mg value of –0.27‰ ±

0.06‰ (2SD; n = 10). Together with inhomogeneous Sr–Nd–Pb–Hf isotopic compositions, the Site U1433 basalts have an average δ26Mg value (–0.20‰ ± 0.06‰; 2SD; n = 8) higher than those of the Site U1431 basalts and normal mantle. Their heavier Mg isotopic compositions and low 206Pb/204Pb ratios (~17.7) indicate that the Site U1433 basalts were affected by the re-melting of detached continental-arc lithosphere in the sub-ridge mantle. The coupling of Mg and Sr–Nd isotopes provides robust evidence that the mantle-like δ26Mg values of the Site U1431 basalts resulted from mixing between detached continental arc lithosphere and the nearby Hainan plume, with respective supra- and sub-normal δ26Mg values. From the perspective of Mg isotope, the mantles of the southwestern and eastern sub-basins are compositionally inhomogeneous, with their mantle evolutionary histories being distinct.

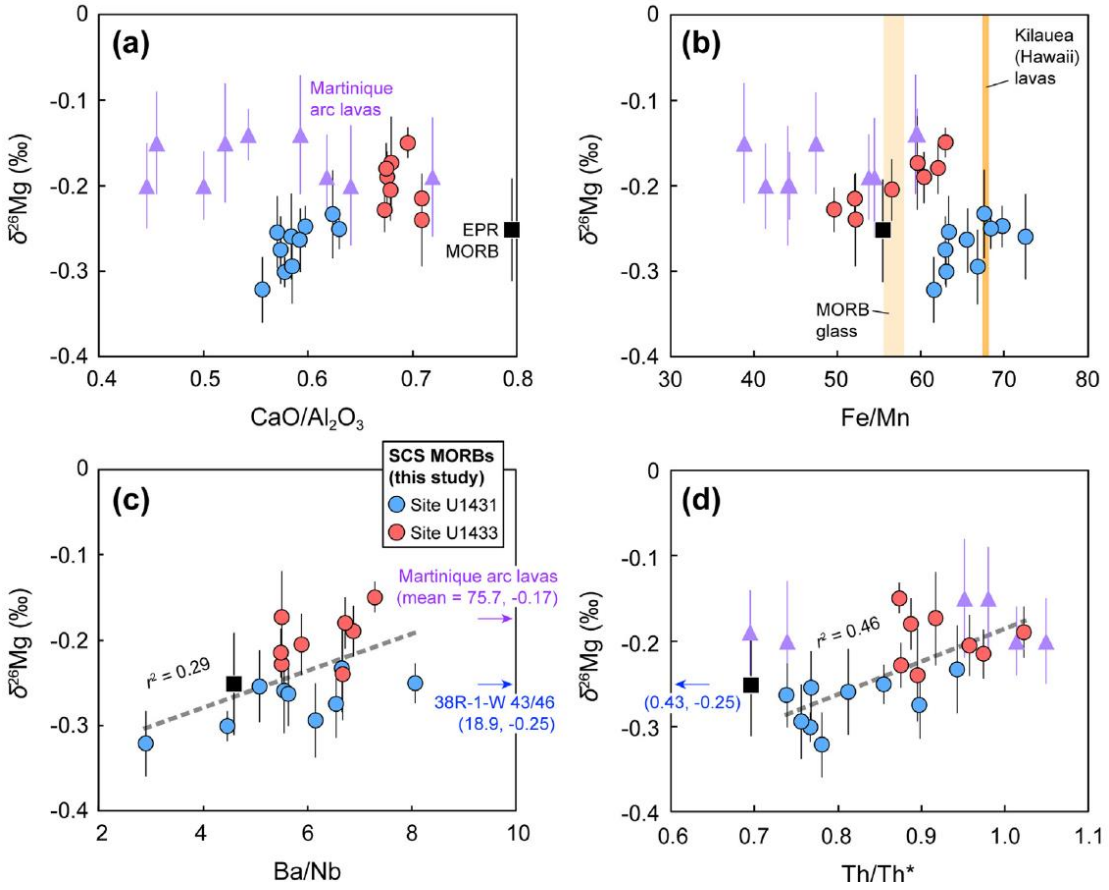

Figure 1. $\delta^{26}Mg$ value versus whole-rock (a) CaO/Al_2O_3, (b) Fe/Mn, (c) Ba/Nb and (d) Th/Th* ratios for SCS MORBs. $Th/Th^* = 2 \times Th_N/(Ba_N + La_N)$, where the subscript N denotes the normalized value with respect to the primitive mantle [62]. The average Mg isotopic composition of EPR MORBs is from Teng et al. [15]; other data are from Gale et al. [46]. To reduce uncertainties in major-element and isotopic compositions caused by magma differentiation and source contamination, only low-silica Martinique arc samples(SiO_2 < 55 wt%) are plotted [35]. Shaded columns in (b) indicate the range of Fe/Mn ratios in oceanic basalts of different source lithology

[63].

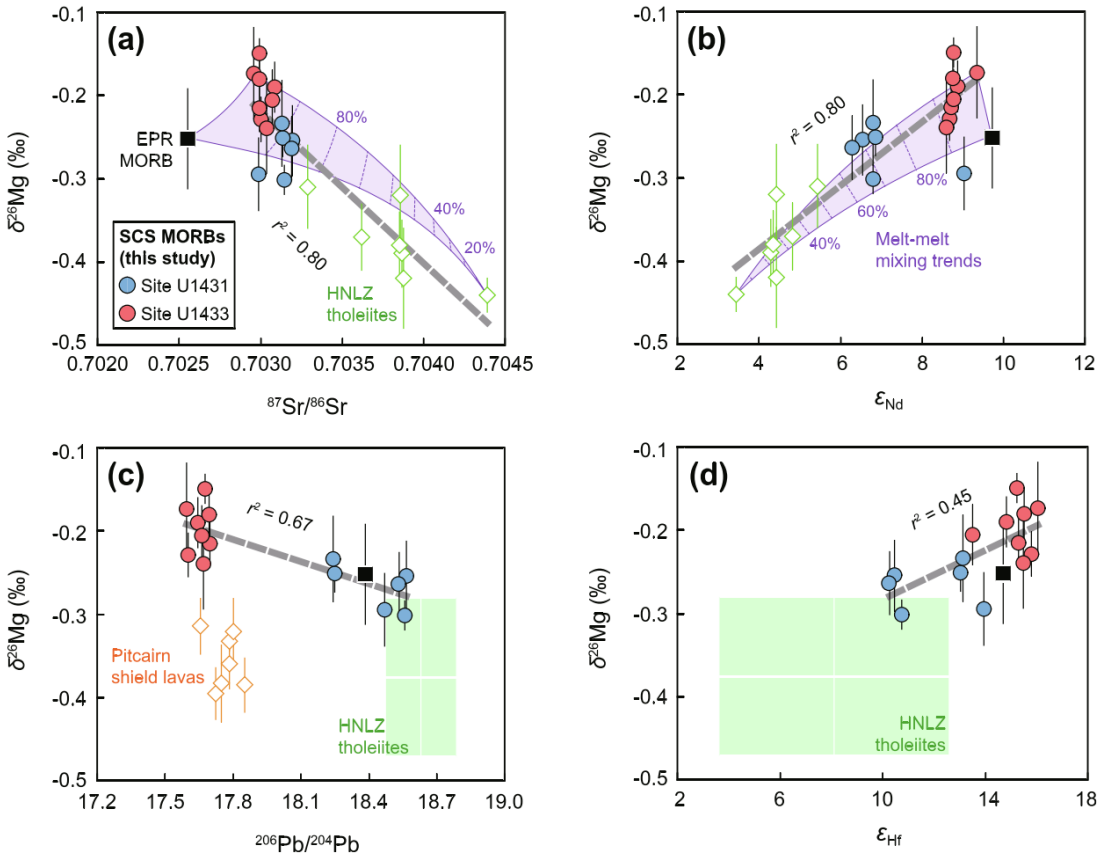

Figure 2. δ^{26}Mg value versus radiogenic Sr–Nd–Pb–Hf isotopic compositions (indicated by $^{87}Sr/^{86}Sr$, ε_{Nd}, $^{206}Pb/^{204}Pb$, and ε_{Hf} values) for SCS MORBs. EPR MORB data are from Teng et al. [15]. Mg and Sr–Nd data for Hainan-Leizhou (HNLZ) tholeiites in (a) and (b) are from Li et al. [12]. The green-shaded areas in (c) and (d) illustrate the means ± 2SD ranges on Mg–Pb–Hf isotopes of HNLZ tholeiites. The corresponding Pb and Hf isotopic data for the HNLZ samples with Mg isotopic compositions are absent and here we use the compiled data from Tu et al. [72], Zou and Fan [73], Wang et al. [74], and Sun et al. [75] instead. Mg and Pb isotopic compositions of Pitcairn shield lavas are from Wang et al. [14]. Purple curves and shaded areas in (a) and (b) depict the melt–melt mixing trends between the Site U1433 MORB (67R-1-W 55/58), HNLZ tholeiite (08HN-5C) and the average EPR MORB with 10% intervals (calculation parameters are given in Table S5 online).

3. 磁学方法研究沿着 Hikurangi 俯冲带边缘马尾状断层的流体富集、迁移和甲烷厌氧氧化

翻译人：李园洁 liyj3@sustech.edu.cn

Greve, A., Kars, M., & Dekkers, M. J. ***Fluid accumulation, migration and anaerobic oxidation of methane along a major splay fault at the Hikurangi subduction margin (New Zealand): A magnetic approach****. Journal of Geophysical Research: Solid Earth, 2021. 126, e2020JB020671.* *https://doi.org/10.1029/2020JB020671*

摘要：理解沿着逆冲断层和马尾状断层的流体流动轨迹对认识增生系统的水力学性质和断层机制具有非常重要的意义。本文，作者利用岩石磁学方法和背散射电子成像描述了 Pāpaku 断层（一个位于 Hikurangi 边缘北部俯冲界面的马尾状断层）内高含量磁性矿物蚀变的轨迹。大洋航次计划的 375 航次在 Pāpaku 断层上 Site U1518 取钻，获得海底下深 250-400 米的室温磁性参数，一阶反转和热磁曲线。~60 米宽的 Pāpaku 破碎带包含两个主要的滑动区：上部脆性(304-321 mbsf)和下部次级(351-361 mbsf) 破碎带，和一个介入区即下部塑性变形带。脆性变形主破碎带顶部的两个窄区域和次级破碎带顶部的含沙层经历了高含量磁性矿物成岩作用，导致了亚铁磁性的硫复铁矿重结晶为顺磁性的黄铁矿。作者推测这一段存在有甲烷和硫化物，厌氧甲烷氧化驱动次生磁性矿物成岩作用。这个变化可能是与断层平行于两个破坏带的流体的迁移导致。上覆的压实的富含粘土的沉积物阻止沿着断层和断层上盘内部的向上对流。

ABSTRACT：Understanding the locus of fluid flow along thrust and splay faults is important to understand the hydraulic properties of accretionary systems and fault mechanics. Here we use rock magnetic techniques in combination with backscattered electron imaging to depict the locus of enhanced magnetic mineral alteration within the Pāpaku fault, an active splay fault of the subduction interface at the northern Hikurangi Margin. The Pāpaku fault was cored at Site U1518 during Expedition 375 of the International Ocean Discovery Program and we report room-temperature magnetic parameters, complemented by First-Order-Reversal and thermomagnetic curves in the depth interval 250-400 meters below seafloor (mbsf). The ~60 m wide Pāpaku fault-zone comprises

two main slip zones, referred to as the upper main brittle (304-321 mbsf) and lower subsidiary (351-361 mbsf) fault zones, and an intervening zoned, termed the lower ductile deformation zone. Two narrow zones, at the top of the mostly brittly deformed main fault zone, and one in a sand-rich interval above the subsidiary fault zone, experienced enhanced magnetic mineral diagenesis, which resulted in the recrystallization of ferrimagnetic greigite to paramagnetic pyrite. We propose that secondary magnetic mineral diagenesis was driven by anaerobic methane oxidation within these intervals, which occurs in the presence of methane and sulfate. We relate the observed changes to the fault parallel transport of fluids which is restricted to two damage zones. Overlying compacted and clay-rich sediments likely act as a barrier to upward advective flow through the fault zone and into the hanging wall.

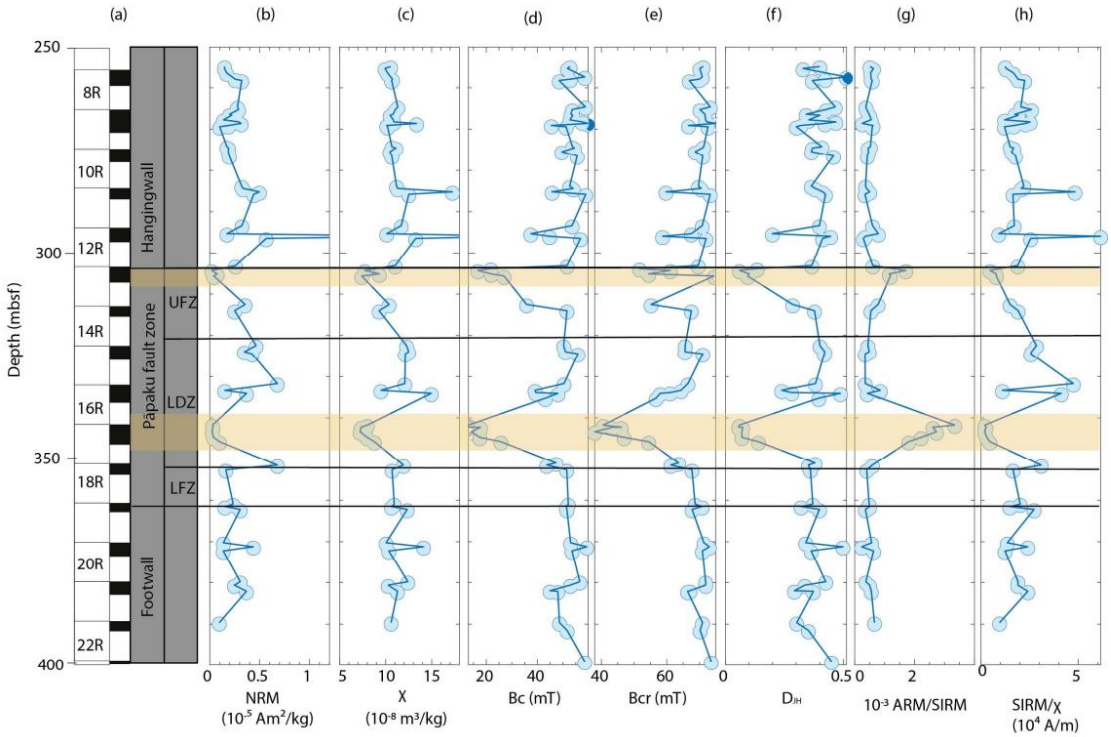

Figure 1. Downcore rock magnetic parameters. (a) core IDs and recovery of core-material (black intervals: core recovered) and structural domains. (b) the Natural Remanent Magnetization (NRM), (c) bulk magnetic susceptibility (χ), (d) the magnetic coercivity (Bc), (e) the coercivity of remanence (Bcr), (f) DJH which is the ratio of the hysteresis parameters DJH= (Mrs/Ms)/(Bcr/Bc) (Housen and Musgrave, 1996), (g) the ratio between the anhysteretic remanent magnetization (ARM) divided by the saturation isothermal remanent magnetization (SIRM), and (h) the ratio between SIRM and χ.

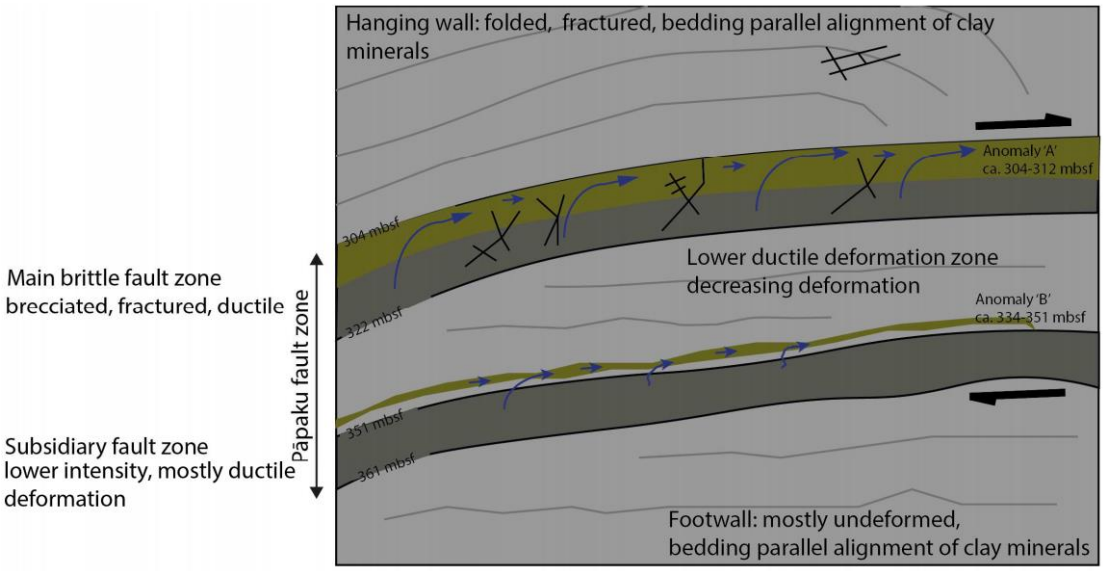

Figure 2. Schematic diagram displaying the main structural domains of the Pāpaku fault zone and inferred fluid migration. In our model we suggest that consolidated hanging wall sediments and compacted, ductilely deformed sediments of the lower ductile deformation zone act as a backstop and result in the accumulation and fault-parallel migration of solutes within two high permeability zones. Anaerobic methane oxidation (AOM) in the presence of methane and sulfate allowed secondary magnetic mineral diagenesis in these intervals (marked in green).

4. 南亚岩浆喷发和平静周期长达 6000 公里的新特提斯岛弧系统

翻译人：周洋 zhouy3@sustech.edu.cn

Zhang X R, Chung S L, Lai Y T, et al. ***A 6000-km-long Neo-Tethyan arc system with coherent magmatic flare-ups and lulls in South Asia*** *[J].* ***Geology****, 2019, v. 47, p. 573–576.*

https://doi.org/10.1130/G46172.1

摘要：岩浆弧通常表现出非稳态演化，具有爆发期和平静期，但主要驱动力仍然存在争议。苏门答腊位于东南亚西南边缘，长期存在一个岩浆弧，其年龄仍然缺乏限制。来自苏门答腊的碎屑锆石数据显示 212、102-85、52 和 22-11 Ma 的年龄峰值。白垩纪至始新世锆石大多产生较高的正 ε Hf（t）值，表明岩浆比较年轻，与南部拉萨地区的冈底斯基岩一致。这些相似之处表明从西藏南部延伸到苏门答腊长约 6000km 的新特提斯岛弧系统，同时表现出岩浆平静期（大约 150–105 Ma 和 85–65 Ma）和岩浆爆发期（大约 105–85 和 65–40 Ma）。晚白垩世岩浆平静期与印度强烈的区域变形和快速北移有关，这可能归因于新特提斯平板俯冲。新特提斯弧岩浆作用的周期性很可能与平板俯冲角度反复变陡和变浅有关，与印度-欧亚大陆的汇聚速度无关。

ABSTRACT: Magmatic arcs typically exhibit non-steady-state evolution with episodic flare-ups and lulls, yet the main drivers remain contentious. Situated in the southwest margin of Southeast Asia, Sumatra records a long-lived magmatic arc that is still poorly constrained in age and tempo. Detrital zircon data from Sumatra delineate major arc magmatic pulses at ca. 212, 102–85, 52, and 22–11 Ma. The mid-Cretaceous to early Eocene zircons mostly yield high positive εHf(t) values, indicating magma derivation from juvenile sources and matching well with those of the Gangdese batholiths in the southern Lhasa terrane. These similarities substantiate an extended (~6000 km) Neo-Tethyan arc system from southern Tibet to Sumatra that exhibits concurrent magmatic lulls (ca. 150–105 and 85–65 Ma) and flare-ups (ca. 105–85 and 65–40 Ma). The Late Cretaceous magmatic lull coincided with a period of strong regional deformation and increasingly fast northward drift of India, likely attributable to Neo-Tethyan flat slab subduction. Periodic pulses of Neo-Tethyan arc magmatism most likely correlated with repeated steepening and shallowing of slab dip, rather than

India-Eurasia convergence rates.

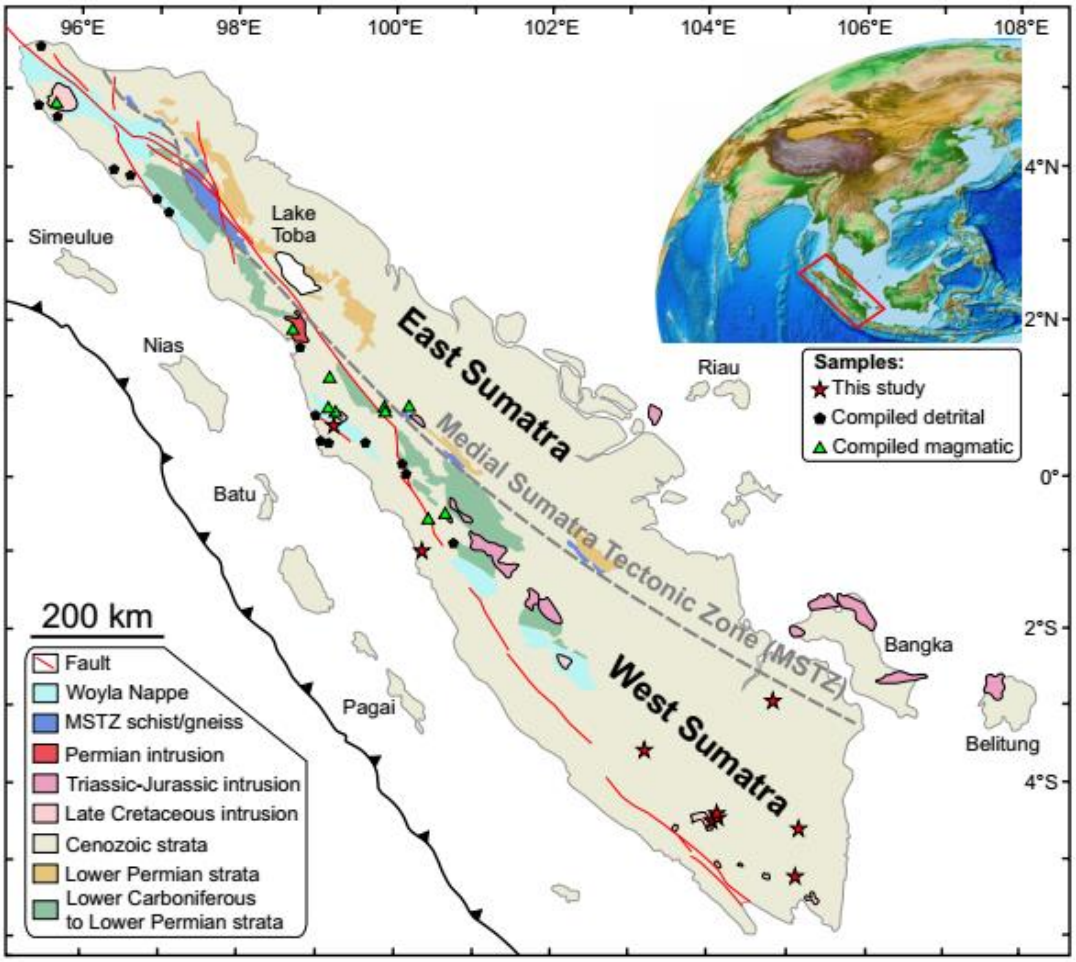

Figure 1. Schematic geological map of Sumatra, modified after Barber et al. (2005). Compiled detrital zircon data are listed in Table DR1 in Data Repository (see footnote 1), and compiled magmatic rocks are from our unpublished results, with zircon εHf(t) values illustrated in Figure 2B.

5. 琉球/小笠原-马里亚纳双重俯冲系统的动力学

翻译人：刘伟 inewway@163.com

Faccenna C , Holt A , Becker T , et al. ***Dynamics of the Ryukyu/Izu-Bonin-Marianas double subduction system****[J].* ***Tectonophysics****, 2017:229-238.*

https://doi.org/10.1016/j.tecto.2017.08.011

摘要：海沟运动反映了俯冲板块与下地幔的相互作用，但其内在的动力学机制尚不完全清楚。一个有趣的例子是 Izu-Bonin-Marianas 海沟(IBM)的迁移，它伴随着菲律宾海板块(PSP)之下的太平洋俯冲，而 PSP 又沿着琉球海沟向欧亚板块之下俯冲。IBM 海沟的历史主要表现为从 40 Ma 到 15 Ma 的快速、偶发性回退。然而，在 10-5 Ma 左右，IBM 海沟的运动从回退转向前进。这种海沟运动的转换发生在 PSP 板块沿琉球海沟断裂和新俯冲开始后不久，代表了西太平洋俯冲带动力学的根本变化。根据 Čížková and Bina (2015) 提出的 IBM 海沟前进和琉球俯冲存在联系的模拟的结果，我们进行二维数值模拟来检验一个新形成的琉球板片对 IBM 俯冲带的影响。我们的地球动力学模型的结果与重建的趋势比较良好，表明 IBM 海沟的运动方向的转换可能确实与沿琉球海沟的新俯冲带的开始有关。我们的分析证实了西太平洋海沟运动的推进是由于双俯冲体系的建立。对这种动力学的进一步分析，将有助于揭示板块和海沟运动的控制机制以及地幔动力的传递作用。

ABSTRACT: Trench motions represent the surface expression of the interaction between subducting plates and the underlying mantle, but the inherent dynamics are not fully understood. One interesting case is the migration of the Izu-Bonin-Marianas trench (IBM) that accommodates the subduction of the Pacific beneath the Philippine Sea Plate (PSP), which is in turn subducting beneath the Eurasian plate along the Ryukyu trench. The history of the IBM trench is dominated by fast, episodic retreat from 40 to 15 Ma. However, around 10–5 Ma, the IBM trench reversed its motion from retreat to advance. The switch in trench motion occurred soon after the breakoff of the PSP slab along the Ryukyu trench and the onset of new subduction, and represents a fundamental change in the dynamics of the western Pacific subduction zones. Here, Following the modelling study of Čížková and Bina (2015), which suggested a link between IBM trench advance and Ryukyu

subduction, we run 2-D numerical experiments to test the influence of a newly formed Ryukyu slab on the established IBM subduction zone, we run two-dimensional numerical experiments to test the influence of this newly formed Ryukyu slab on the IBM subduction zone. The results from our geodynamic model compare favourably with the reconstructed trend, indicating that the switch in trench motion along the IBM trench may indeed be related to the onset of a new subduction zone along the Ryukyu trench. Our analysis substantiates the idea that advancing trench motions in the western Pacific are due to the establishment of a double subduction system. Further analysis of such dynamics provides insights for the mechanisms controlling subducting plate and trench motions and mantle force transmission.

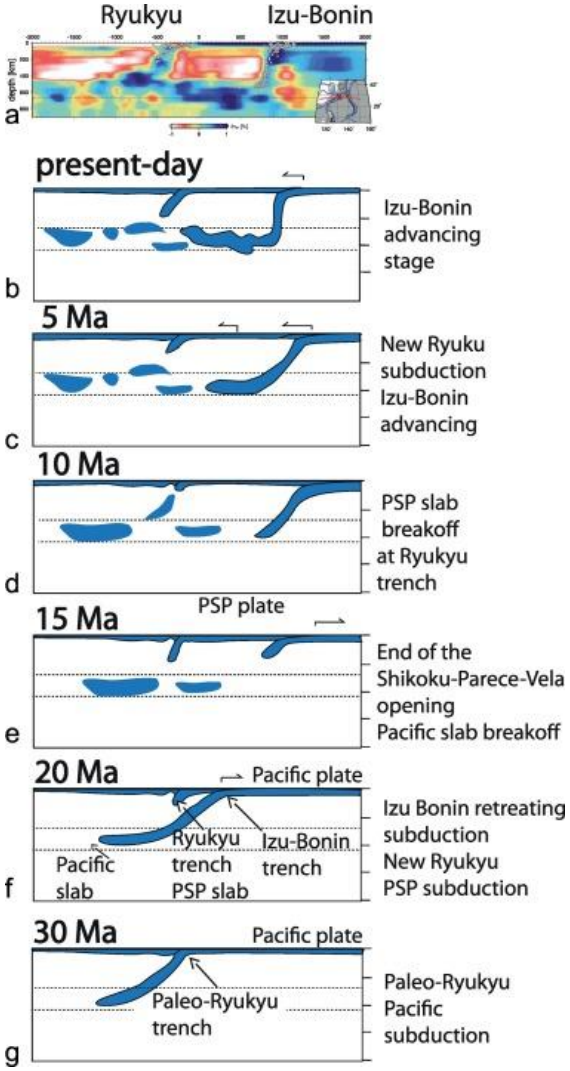

Figure 1. Possible reconstruction of along a cross section at 26° N (Fig. 2) of the mantle structure. a) Tomography model from Li et al. (2008); b–g) six stage evolution of the subduction zone. The subduction zone has been restored backward in time considering the position of the trench and the subduction velocity as from plate motion of Seton et al. (2012). PSP is Philippine Sea Plate.

6. 亚洲季风自中更新世以来的季节性干湿变化

翻译人：杨会会 11849590@mail.sustech.edu.cn

Wang X, Dettman D L, Wang M and et al. ***Seasonal wet-dry variability of the Asian monsoon since the middle Pleistocene****[J]* ***Quaternary Science Reviews****,247,106568*

https://doi.org/10.1016/j.quascirev.2020.106568

摘要：夏季多雨和冬季干燥是季风气候的一个基本特征，但由于大多数地质材料无法记录亚年尺度环境信号，而是整年，十年或者百年尺度环境信号，因此量化干湿季节随时间的变化非常具有挑战性。本文我们通过黄土高原陆螺壳高分辨率稳定氧同位素分析定量化研究中更新世以来亚洲干湿季节变化。这种方法使我们能够收集地质历史上单一季节和年份的数据。现代的蜗牛壳体表明：（1）北半球冬(干)季 $\delta^{18}O_{shell}$ 值较高，夏(湿)季 $\delta^{18}O_{shell}$ 值较低；（2）$\delta^{18}O_{shell}$ 冬夏季同位素差达 19.2‰，远高于季节气温变化的预期值；（3）蜗牛壳内的 $\delta^{18}O_{shell}$ 变化(最正和最负的差值)记录了旱季蜗牛体内水的蒸发程度，指示了雨季降雨 $\delta^{18}O$/温度。这一变化可以作为一个干湿季节性的指标，尽管很明显需要更多的工作来校准这个指标。冰期黄土层中 $\delta^{18}O_{shell}$ 的变化范围（平均值=13.6‰）系统性地比间冰期黄土中 $\delta^{18}O_{shell}$（平均值=8.6‰）的变化范围要大，表明中更新世以来，冰期冬季更干燥，而间冰期冬季更湿润。这种模式可能是冰期干燥的西风带入侵该地区导致的。在整个记录中夏季最小 $\delta^{18}O_{shell}$ 值是相似的，与石笋冰期/间冰期记录的对比明显，尤其是如果这些代表了典型的季风降雨的稳定同位素模式。然而，如果一些来自西风带的水分在冰期贡献了更多的负 $\delta^{18}O$ 值，这些最小 $\delta^{18}O$ 值可能与洞穴记录中的模式不矛盾。今后的研究工作应集中在陆生螺壳同位素周期的季节性。

ABSTRACT: Wet summers and dry winters are an essential feature of monsoon climates, but quantification of change in wet-dry seasonality through time is very challenging because most geological materials fail to record sub-annual environmental signals, instead integrating years, decades, or centuries. Here we quantify Asian wet-dry seasonality since the middle Pleistocene for monsoon climates using high-resolution stable oxygen isotope analysis of land snail shells from the Chinese Loess Plateau. This approach allows us to collect data on single seasons and years in geologic history. Modern shells show that: 1) the $\delta^{18}O_{shell}$ values are higher in boreal winter (dry)

seasons and lower in boreal summer (wet) seasons; 2) winter e summer differences in $\delta^{18}O_{shell}$ (up to 19.2‰) are much larger than that expected from seasonal temperature variation; and 3) the $\delta^{18}O_{shell}$ range (the difference between the most positive and the most negative values) within a shell records the degree of evaporation of snail body water in the dry season, combined with a rainfall $\delta^{18}O$/temperature indicator in the wet season. This range can be used as a wet/dry seasonality proxy index, although clearly more work is required to calibrate this index. $\delta^{18}O_{shell}$ ranges in glacial loess strata (mean = 13.6‰) are systematically larger than those from interglacial paleosol layers (mean = 8.6‰), suggesting that a significant difference in winter aridity was present, with drier winters in glacial periods and wetter winters in interglacial periods since the middle Pleistocene. This pattern may have been modified by the intrusion of the westerlies into the region in glacial dry seasons. Summer minimum $\delta^{18}O_{shell}$ values are similar throughout the record, which contrasts significantly with glacial/interglacial speleothem records, especially if these represent typical monsoon stable isotope patterns in rains. However, if some moisture from the westerlies contribute more negative $\delta^{18}O$ values in glacial intervals, these minimum $\delta^{18}O$ values may not contradict the patterns seen in the speleothem record. Future work should focus on the seasonal timing of the isotope cycles in land snail shells.

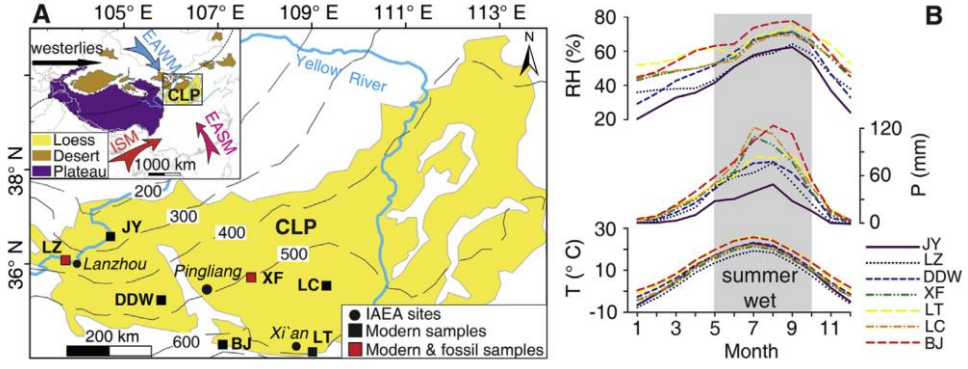

Figure 1. Map showing the prevailing monsoon climate regime on the Chinese Loess Plateau and sampling sites. Isohyets (in mm, dashed gray lines) are from rainfall dataset of National Meteorological Information Center (http://data.cma.cn/) for 1981-2010 with horizontal resolution of 2.5°. The black dashed line in inset indicates the northern boundary of the Asian monsoon rain belt (Chen et al., 2015). Abbreviations: LZ, Lanzhou; JY, Jingyuan; DDW, Dadiwan; XF, Xifeng; BJ, Baoji; LC, Luochuan; LT, Lantian; ISM, Indian Summer Monsoon; EASM, East Asia Summer Monsoon; EAWM, East Asia Winter Monsoon; T, Temperature; P, Precipitation; RH, Relative humidity.

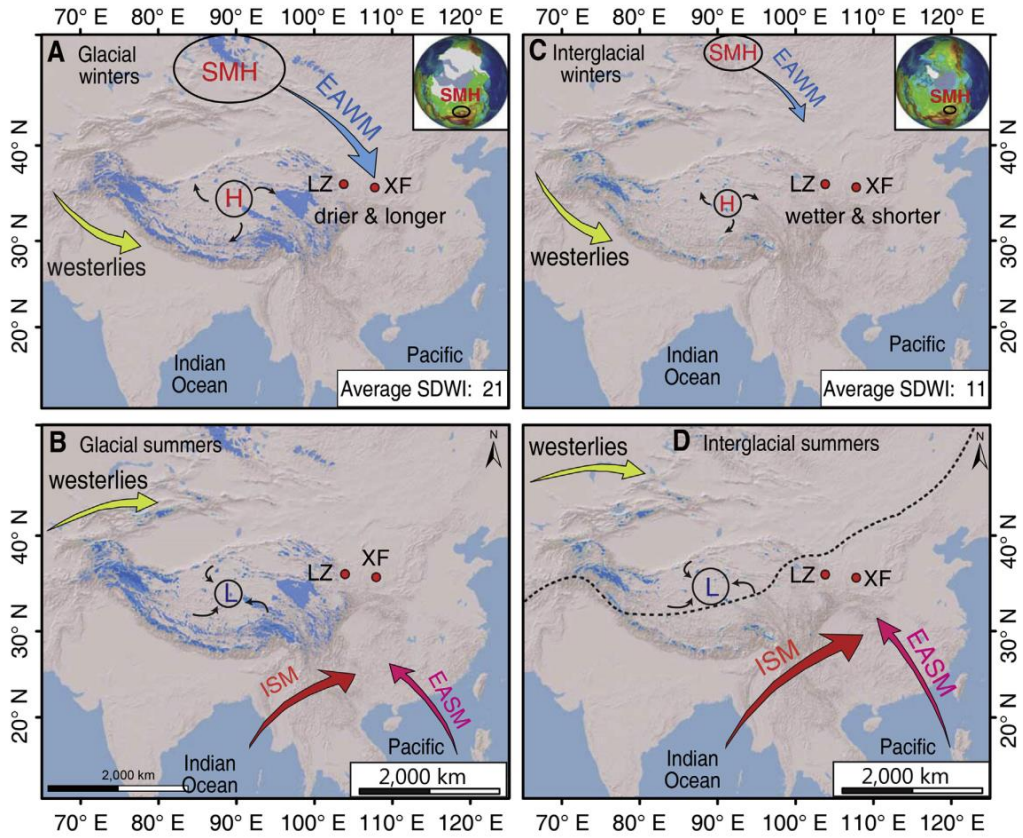

Figure 2. Schematic maps showing dynamics of Asian paleomonsoon on a seasonal scale for glacial (A-B) and interglacial (C-D) periods since middle Pleistocene. Ice cover (solid blue areas) for LGM and present day are cited from Ehlers et al. (2011). The dashed line in (D) indicates the northern boundary of the modern summer rain belt (Chen et al., 2015). Abbreviations: SMH, Siberian-Mongolian High; ISM, Indian Summer Monsoon; EASM, East Asia Summer Monsoon.

7. 利用 Burry XII 型分布分解剩余磁化曲线

翻译人：王敦繁 dunfan-W@foxmail.com

Zhao, X.Y., Fujii, M., Suganuma, Y., Zhao, X., & Jiang, Z. (2018). ***Applying the Burr type XII distribution to decompose remanent magnetization curves****. Journal of Geophysical Research: Solid Earth, 123*

https://doi.org/ 10.1029/2018JB016082

摘要：通过剩余磁化曲线的分析，可以区分自然样品中不同来源的磁性矿物，有助于揭示其相关的地质和环境过程。分离混磁性组分有赖于对模型分布的选择来。以往的研究提出了三种模型分布，即对数正态分布、偏态正态分布和偏态广义高斯分布，它们与正态分布有关。本研究对 XII 型 Burr 分布进行了检验，并与现有模型分布进行了比较。提出了一种自动分配参数以启动组份分析的方法，提高了效率和客观性。结果表明，新的模型分布在逼近偏斜正态分布和偏斜广义高斯分布时具有相似的灵活性，并且比常用的对数正态分布更能拟合端元分量。我们证明了成分分析对模型分布和测量噪声都是敏感的。由于缺乏地面真实数据，分解容易产生偏差，难以识别。因此，建议同时比较来自各种模型分布的结果，以识别虚假组分。

ABSTRACT: To Discriminating magnetic minerals of different origins in natural samples is useful to reveal their associated geological and environmental processes, which can be achieved by the analysis of remanent magnetization curves. The analysis relies on the choice of the model distribution to unmix magnetic components. Three model distributions were proposed in past studies, namely, the lognormal, skew normal, and skewed generalized Gaussian distributions, which are related to the normal distribution. In this study, the Burr type XII distribution is tested and compared with existing model distributions. An automated protocol is proposed to assign parameters necessary to initiate the component analysis, which improves the efficiency and objectivity. Results show that the new model distribution exhibits similar flexibility to the skew normal and skewed generalized Gaussian distributions in approximating skewed coercivity distributions and can fit end-member components better than the commonly used lognormal distribution. We demonstrate that the component analysis is sensitive to model distribution as well as measurement noise. As a

consequence, the decomposition is subject to bias that is hard to identify due to the lack of ground-truth data. It is therefore recommended to compare results derived from various model distributions to identify spurious components.

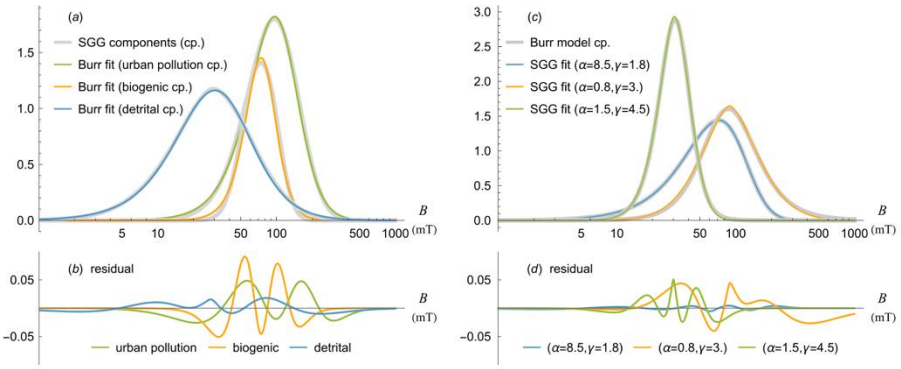

Figure 1. Comparison between the Burr type XII distribution and the skewed generalized Gaussian (SGG) distribution. (a) The SGG components (gray lines, from Egli (2004a)) and best fits of the Burr type XII distributions (colored lines) with the following shape parameters (α, γ): detrital cp (α = 1.517, γ = 1.806), biogenic cp (α = 1.446, γ = 4.568), and urban pollution cp (α = 2.055, γ = 2.657). (b) Corresponding residuals. (c) Best fits of the SGG distribution (colored lines) to the modeled Burr components (gray lines). Shape parameters for modeled components are shown in legends. (d) Corresponding residuals. Note that cp means component.

8. 1500 BCE--150 CE 地中海中部的地磁场强度变化

翻译人：李海 12031330@mail.sustech.edu.cn

Rivero-Montero, M., Gómez-Paccard, M. et al., 2021. ***Geomagnetic field intensity changes in the Central Mediterranean between 1500 BCE and 150 CE: Implications for the Levantine Iron Age Anomaly evolution.*** *Earth and Planetary Science Letters, 557: 116732.*

https://doi.org/10.1016/j.epsl.2020.116732

摘要: 对于黎凡特铁器时代地磁异常（LIAA）的大小和异常，目前还没有很好的了解。来自黎凡特和西欧最新的古地磁研究表明，该特征正发生西向漂移，进而强调了在地中海地区调查这一事件的时空重要性。为此，我们从希腊和意大利的8个考古遗址中收集了118个陶瓷和碎砖片进行古强度测试，获得37个新的古地磁强度数据，年代从公元前1500年至公元150年。使用经典的Thellier and Thellier方法进行古强度的测定，包括矫正热磁化强度的各向异性以及冷却速率的影响。结果显示，希腊在1070 BCE至1040 BCE间出现高强度峰值，与虚轴偶极矩的高值相对应。对全球可用的古强度数据进行分析表明，这些高值的起源与在黎凡特地区产生LIAA的最大VADM的那些相同。我们的结果表明LIAA来源于黎凡特地区，并向东、北、西降低。此外，整个欧洲在公元前500年左右出现了另一个古强度峰值。这两个事件似乎都跨越了地球表面的一个大区域，覆盖了超过60°的经度，这证实了这些强度特征的地球外核起源。

ABSTRACT: The magnitude and origin of the Levantine Iron Age geomagnetic Anomaly (LIAA), which spanned the first half of the first millennium before the common era, are not yet well understood. Recent archeomagnetic studies from the Levant and Western Europe suggest a western drift of this feature, stressing the importance of investigating the temporal and spatial behaviour of this event over the Central Mediterranean area. To analyse this issue, we here present 37 new archeointensity data obtained from the archeomagnetic study of 118 ceramics and brick fragments collected in 8 archeological sites in Greece and Italy with ages ranging between 1500 BCE and 150 CE. The samples were analysed using the classical Thellier and Thellier method for paleointensity determination, including the correction for the anisotropy effect of the thermoremanent magnetization (TRM) and for the cooling rate dependence upon TRM acquisition. The results reveal

the first evidence of a high-intensity peak in Greece between 1070 and 1040 BCE associated to high virtual axial dipole moment (VADM) values of around 140 ZAm2. A global analysis of available paleointensities suggests that the origin of these high values is the same to the one which produced the maximum VADM of the LIAA in the Levantine region. Our results suggest that the source of the LIAA is located in the Levantine region vanishing to the north, to the west and to the east where lower VADMs are observed. In addition, another high intensity maximum, less pronounced than the one of the LIAA, seems to be present around 500 BCE all over Europe, from the Canary Islands to Turkey showing similar VADM values (around 150 ZAm2) in the different regions. Both events seem to span over a large region at the Earth's surface covering more than 60° of longitude, verifying an Earth's outer core origin for these intensity features.

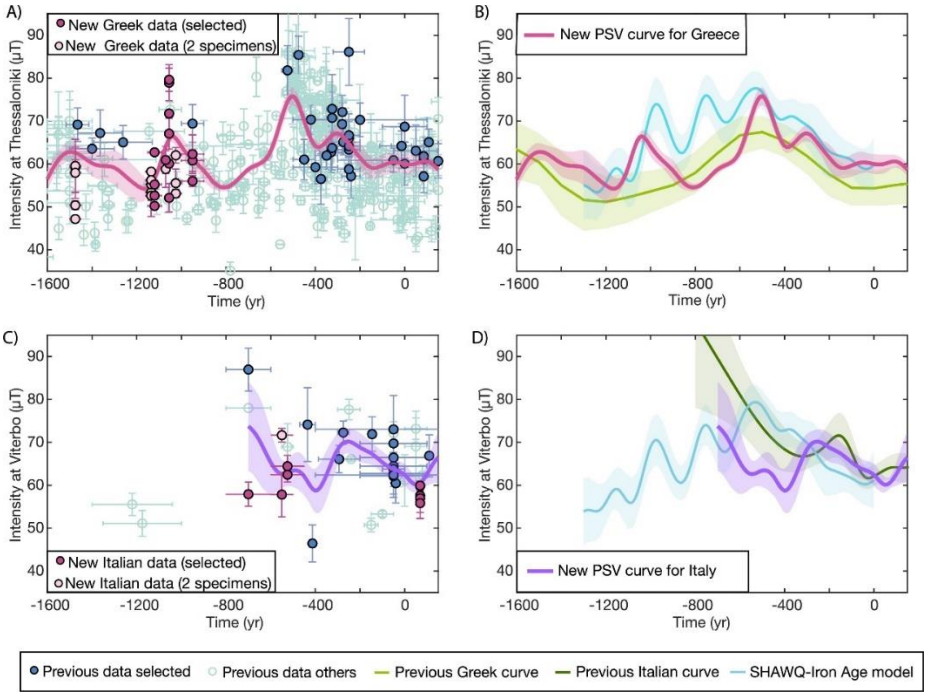

Figure 1. (Left panels) New archeointensity results (pink circles) obtained for the Central Mediterranean. Dark pink circles correspond to data obtained from 3 or more specimens, and light pink circles correspond to data with 2 specimens. Our new data are compared with previous data (greenish blue). Data plotted in dark colours correspond to those that pass the selection criteria applied in this study (see text for further details). All data are relocated to Thessaloniki (40.63°N, 22.95°E) for Greece and Viterbo (42.45°N, 12.03°E) for Italy. The new PSV curves obtained for Greece and Italy (pink and violet lines) together with its 1-sigma error band (shaded areas) are also showed. (Right panels) Comparison of the new curves with the previous versions (De Marco et al., 2008; Tema and Lanos, 2020, for Greece and Italy respectively) and with the prediction of the global geomagnetic field model SHAWQ-Iron Age (Osete et al., 2020).

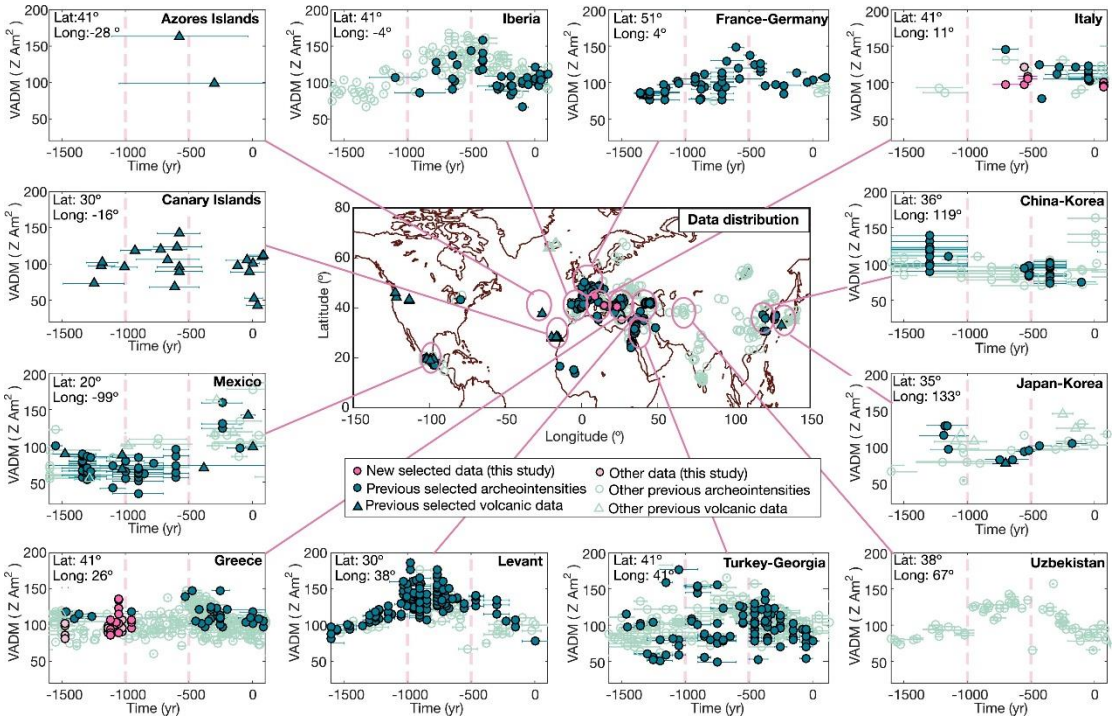

Figure 2. VADMs for different regions represented by pink circles in the central map. Dark (light) colours correspond to data that pass (do not pass) the selection criteria applied in this study (see main text). The new data obtained here are shown in pink and previous data from other studies in greenish blue. Dashed lines at 1000 BCE and 500 BCE are only marked for visual reference.

9. 中新世以来由吕宋海峡的形成造成南海与北太平洋亚热带环流的隔离

翻译人：张亚南 zhangyn3@mail.sustech.edu.cn

Shaoru Yin, F. Javier Hernández-Molina, Lin Lin et al. ***Isolation of the South China Sea from the North Pacific Subtropical Gyre since the latest Miocene due to formation of the Luzon Strait*** *[J].* ***Scientific Reports****, 2021,11, 1562.*

https://doi.org/10.1038/s41598-020-79941-4

摘要：北太平洋副热带环流（NPSG）在现今全球海洋环流中起着重要的作用。有时 NPSG 会穿过南海，但在该海域中演化发展中的作用仍不确定。本文系统地描述了从地震和水深观测资料中所观察到的沉积特征，其反应了 NPSG 古环流的重大变化。这些数据勾勒出两种等深流沉积体系：一种是晚中新世晚期埋藏的，另一种中新世末期—现在沉积的。着两个趁机体系被明显的区域不整合划分开，代表了中新世末期（~6.5Ma）古环流的重大转变。这一转变与菲律宾板块进一步向西北移动，使得吕宋海峡形成，从而使得南海进一步的受限相一致。在此之前，数据表明 NPSG 环流在南海十分活跃，然而在中新世晚期，半封闭性南海的形成建立了新的海洋环流体系。这一工作说明了板块构造、通道发育和边缘海在建立现代全球海洋环流中的重要作用。

ABSTRACT: The North Pacific subtropical gyre (NPSG) plays a major role in present global ocean circulation. At times, the gyre has coursed through the South China Sea, but its role in the evolutionary development of that Sea remains uncertain. This work systematically describes a major shift in NPSG paleo-circulation evident from sedimentary features observed in seismic and bathymetric data. These data outline two contourite depositional systems—a buried one formed in the late Miocene, and a latest Miocene to present-day system. The two are divided by a prominent regional discontinuity that represents a major shift in paleo-circulation during the latest Miocene (~ 6.5 Ma). The shift coincides with the further restriction of the South China Sea with respect to the North Pacific due to the formation of the Luzon Strait as a consequence of further northwest movement of the Philippine Sea plate. Before that restriction, data indicate vigorous NPSG circulation in the South China Sea. Semi-closure, however, established a new oceanographic circulation regime in the latest Miocene. This work demonstrates the significant role of recent plate

tectonics, gateway development, and marginal seas in the establishment of modern global ocean circulation.

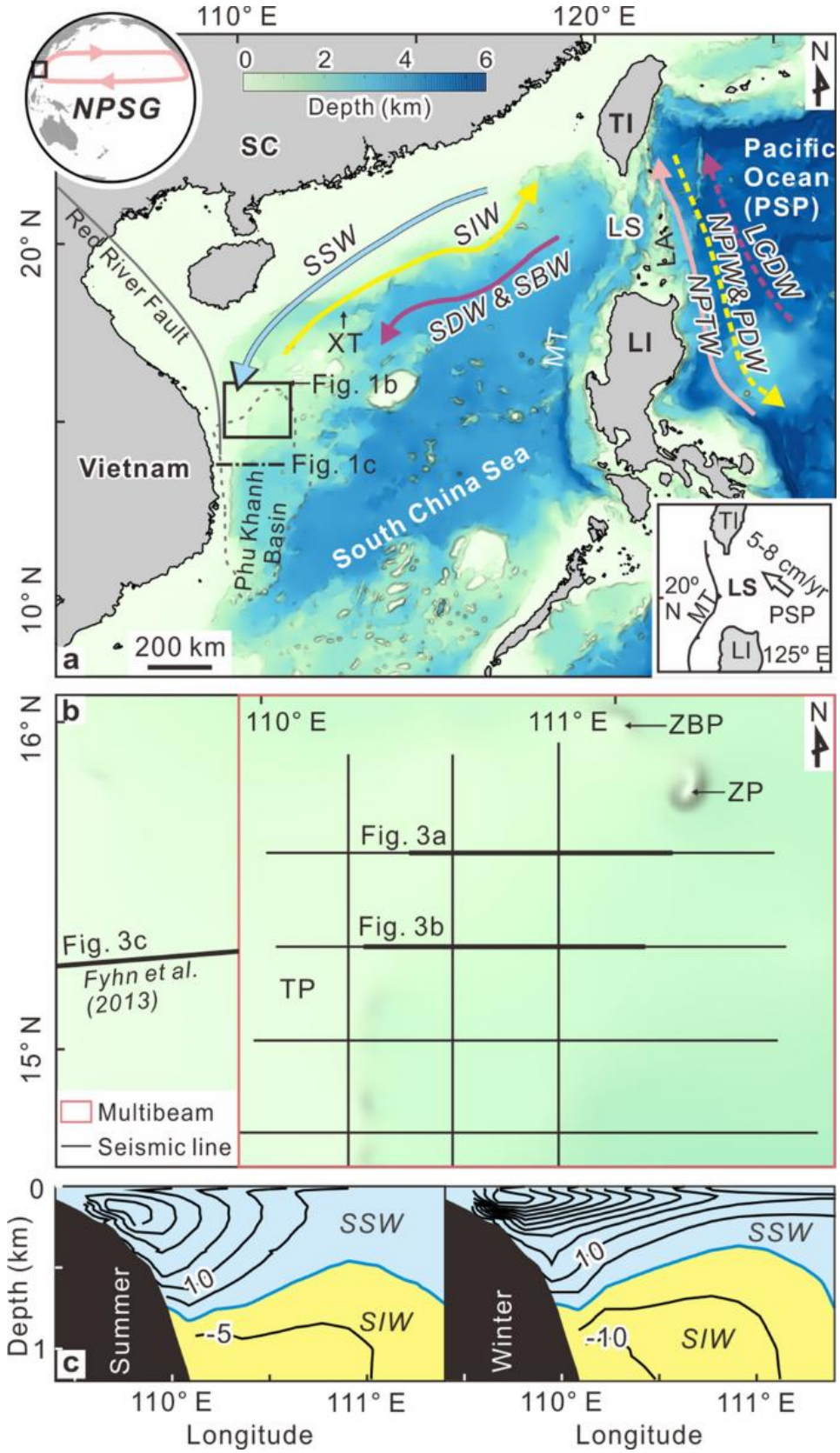

Figure 1. (a) Study area location (black rectangle) including water mass circulation. The black arrow

marks the sense of movement of the plate. The gray line shows the location of Red River Fault. Dotted gray lines show the boundaries of Phu Khanh basin. Dotted-dashed line marks the hydrographic line in panel (c); (b) data used in this study, including bathymetric survey and surface trace of seismic surveys; and (c) observations of 20-year average current velocity (cm/s) from 1992 to 2011 (data were provided by Huijie Xue), where positive velocity values denote southward flow and negative values denote northward flow. The blue line marks the zero contours. Contour interval is 5 m. TI Taiwan Island, LI Luzon Island, PSP Philippine Sea plate, LS Luzon Strait, LA Luzon arc, SC South China, MT Manila Trench, XT Xisha Trough, TP Triton platform, ZP Zhongjian platform, ZJB Zhongjianbei platform. Abbreviations for water masses given in text.

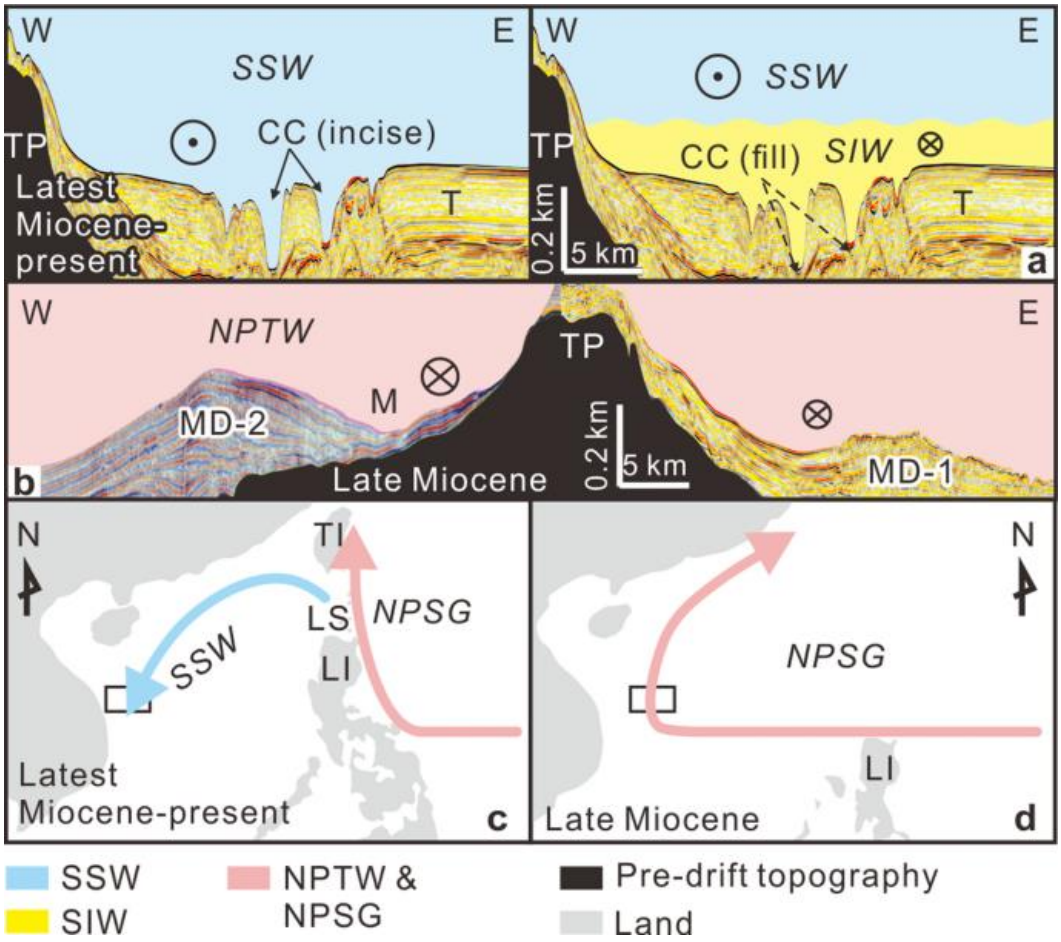

Figure 2. Sketches for the terrace and the contourite depositional systems for SU2 (a) and SU1 (b) formation under South China Sea circulation. Reconstruction of circulation from latest Miocene to present (c) and in late Miocene (d). In panels (a,b), current direction is indicated by the symbols: circled times = Northward flow and circled dot = Southward flow. Topography data source in (c) is ETOPO1 (https://doi.org/10.7289/V5C8276M, https://ngdc.noaa.gov/mgg/global/global.html). Topography in (d) is modified from Hall, 20124. Abbreviations for water masses given in text. Abbreviations for sedimentary features referenced to Fig. 2. Seismic images in (a,b) were generated using GeoFrame software (version 4.5, http://slb-sis.com.cn/products-services/GeoFrame.aspx). All maps were designed using CorelDraw Graphics Suite X8 (https://www.coreldraw.com/cn/).

10. 利用量子金刚石显微镜(QDM)进行高分辨率环境磁学研究:在热带洞穴堆积物中的应用

翻译人：张伟杰 12031188@mail.sustech.edu.cn

Fu RR, Hess K, Jaqueto P, Novello VF, Kukla T, Trindade RIF, Strikis NM, Cruz FW and Ben Dor O (2021) ***High-Resolution Environmental Magnetism Using the Quantum Diamond Microscope (QDM): Application to a Tropical Speleothem****. Front. Earth Sci. 8:604505.*
https://doi.org/10.3389/feart.2020.604505

摘要：量子金刚石显微镜(QDM)磁场成像技术是近年来发展起来的一种以 1 微米分辨率绘制地质样品中磁场源的技术。将 QDM 成像应用于洞穴生物可以提供洞穴环境碎屑输入的高分辨率时间序列，从而可以提供有用的古环境信息。本文，我们用年到次年分辨率绘制了 174 年时间跨度的巴西中西部洞穴的磁场，并进行了反向场剩磁获取实验，以量化磁性颗粒随时间的变化。我们发现磁性颗粒存在于 10-100 μm 厚的高富集层中，这些层具有相同的碎屑来源。结合岩相观察和镁、钙的电子探针分布图，我们得出结论:岩屑在样品中的富集是由于干燥条件导致洞穴生长缓慢或停止。这一解释与氧同位素数据是一致的，这意味着洞穴堆积物磁性可以用来推断过去发生的干旱，并可能量化其持续时间。未来穴堆积物的高分辨率磁成像可能为碎屑富集的机制提供另外的见解，并确定其作为当地水分和渗透的代用指标。

ABSTRACT: Quantum diamond microscope (QDM) magnetic field imaging is a recently developed technique capable of mapping magnetic field sources in geologic samples at 1 micrometer resolution. Applying QDM imaging to speleothems can provide high-resolution time series of detrital input into the cave environment, which, in turn, can yield useful paleoenvironmental information. Here we map the magnetic field over a speleothem from midwest Brazil over a 174 year timespan with annual to sub-annual resolution and perform backfield remanence acquisition experiments to quantify changes in the magnetic grain population through time. We find that magnetic particles occur in highly enriched layers of 10–100 μm thickness that sample the same detrital source population. Combined with petrographic observations and electron microprobe mapping of Mg and Ca, we conclude that detrital enrichment in our sample is caused by drier conditions leading to slow or halted speleothem growth. This interpretation is compatible with oxygen isotopic data and implies that speleothem magnetism can be used to infer the past occurrence of drought and potentially quantify their duration. Future high-resolution magnetic imaging of speleothems may provide additional insight into the mechanism of detrital enrichment

and establish their role as a proxy for local moisture and infiltration.

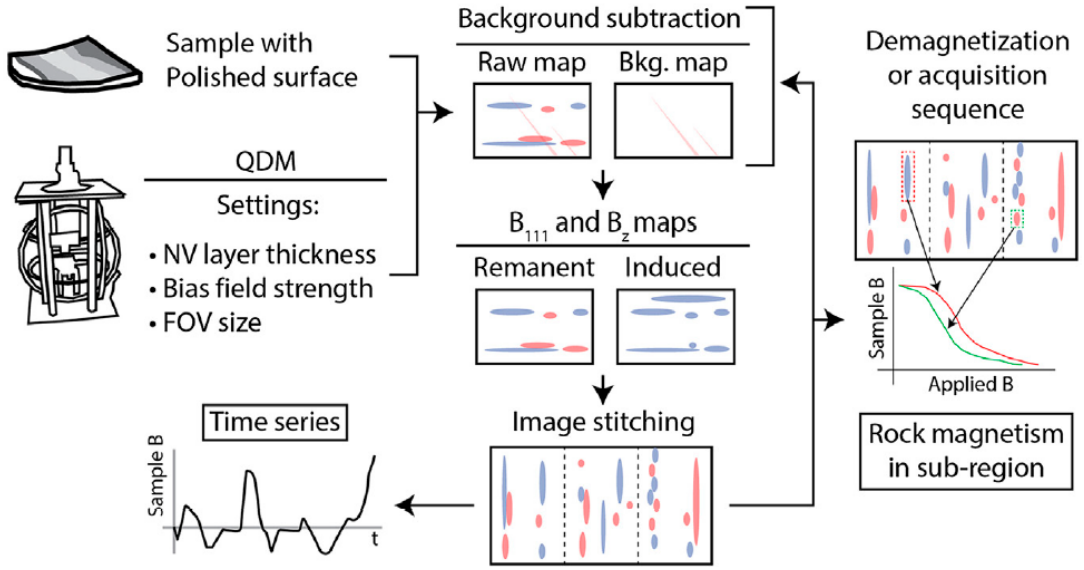

Figure 1. Flowchart summary of experimental procedure. After we obtain a raw map of the magnetic field in the <111> crystallographic direction (B111), we apply background subtraction where necessary, convert to Bz using a Fourier domain transform, and stitch adjacent fields of view using the optical image associated with each magnetic field map. A time series of magnetic field strength, which is a proxy for magnetization, can be obtained with an age model. Repeated imaging of the same field(s) of view combined with a demagnetization or remanence acquisition sequence can be used to construct demagnetization or acquisition curves for small subregions.

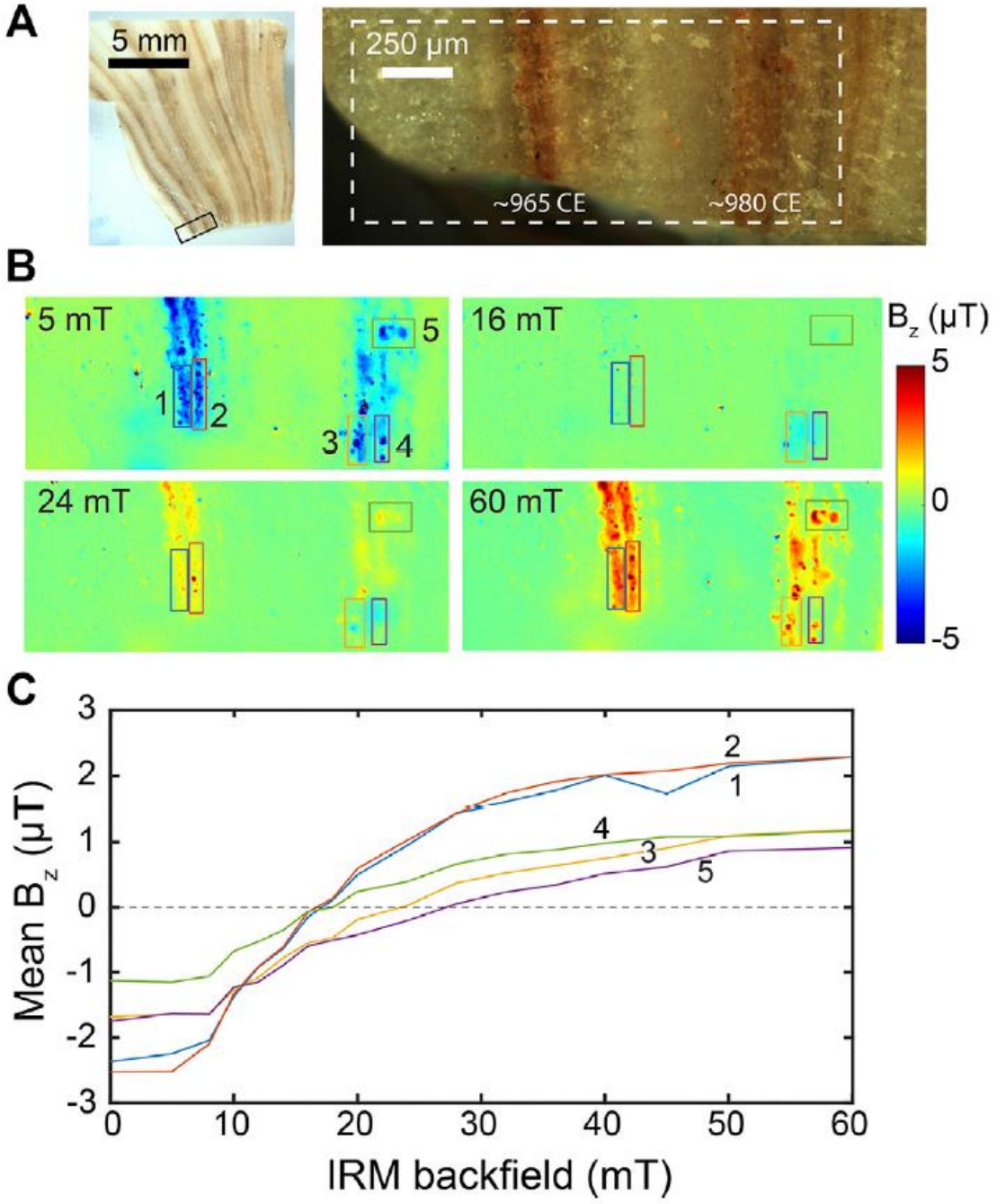

Figure 2. Backfield IRM acquisition experiment from one field of field. (A) Reflected light, crossed polarizer images of the mapped region. (B) Vertical component of the magnetic field after the application of a 1.5 pulse IRM into the mapping plane and an IRM of the indicated strength out of the plane. Mapped region corresponds to white dashed box in panel (A). (C) Backfield IRM acquisition curves of the five rectangular regions indicated in panel (B).

11. 葫芦洞记录的末次冰期以来大气 $^{14}C/^{12}C$ 变化

翻译人：柳加波 Liujb@sustech.edu.cn

Cheng H, Edwards R L, Southon J, et al. ***Atmospheric 14C/12C changes during the last glacial period from Hulu Cave[J]****. Science, 2018, 362(6420): 1293-1297.*

https://doi.org/10.1126/science.aau0747

摘要：对葫芦洞两根石笋进行 $^{14}C/^{12}C$ 和 ^{230}Th 年龄进行配对测量，获得了完整的约 54,000 年（14C 测量范围）以来的大气 ^{14}C 精确记录。末次冰期期间，大气 $^{14}C/^{12}C$ 的值在接近现代值到现代值的 1.70 倍（42,000 到 39,000 年前）之间的范围内波动。后者对应的 ^{14}C 年龄比校正年龄少 5200 年，这与 Laschamp 地磁漂移以及 Heinrich Stadial 4 气候事件有关。$^{14}C/^{12}C$ 值在 25,000 到 11,000 年前不断降低，这可能部分与逐渐上升的海洋通风率有关。

ABSTRACT: Paired measurements of $^{14}C/^{12}C$ and ^{230}Th ages from two Hulu Cave stalagmites complete a precise record of atmospheric ^{14}C covering the full range of the ^{14}C dating method (~54,000 years). Over the last glacial period, atmospheric $^{14}C/^{12}C$ ranges from values similar to modern values to values 1.70 times higher (42,000 to 39,000 years ago). The latter correspond to ^{14}C ages 5200 years less than calibrated ages and correlate with the Laschamp geomagnetic excursion followed by Heinrich Stadial 4. Millennial-scale variations are largely attributable to Earth's magnetic field changes and in part to climate-related changes in the oceanic carbon cycle. A progressive shift to lower $^{14}C/^{12}C$ values between 25,000 and 11,000 years ago is likely related, in part, to progressively increasing ocean ventilation rates.

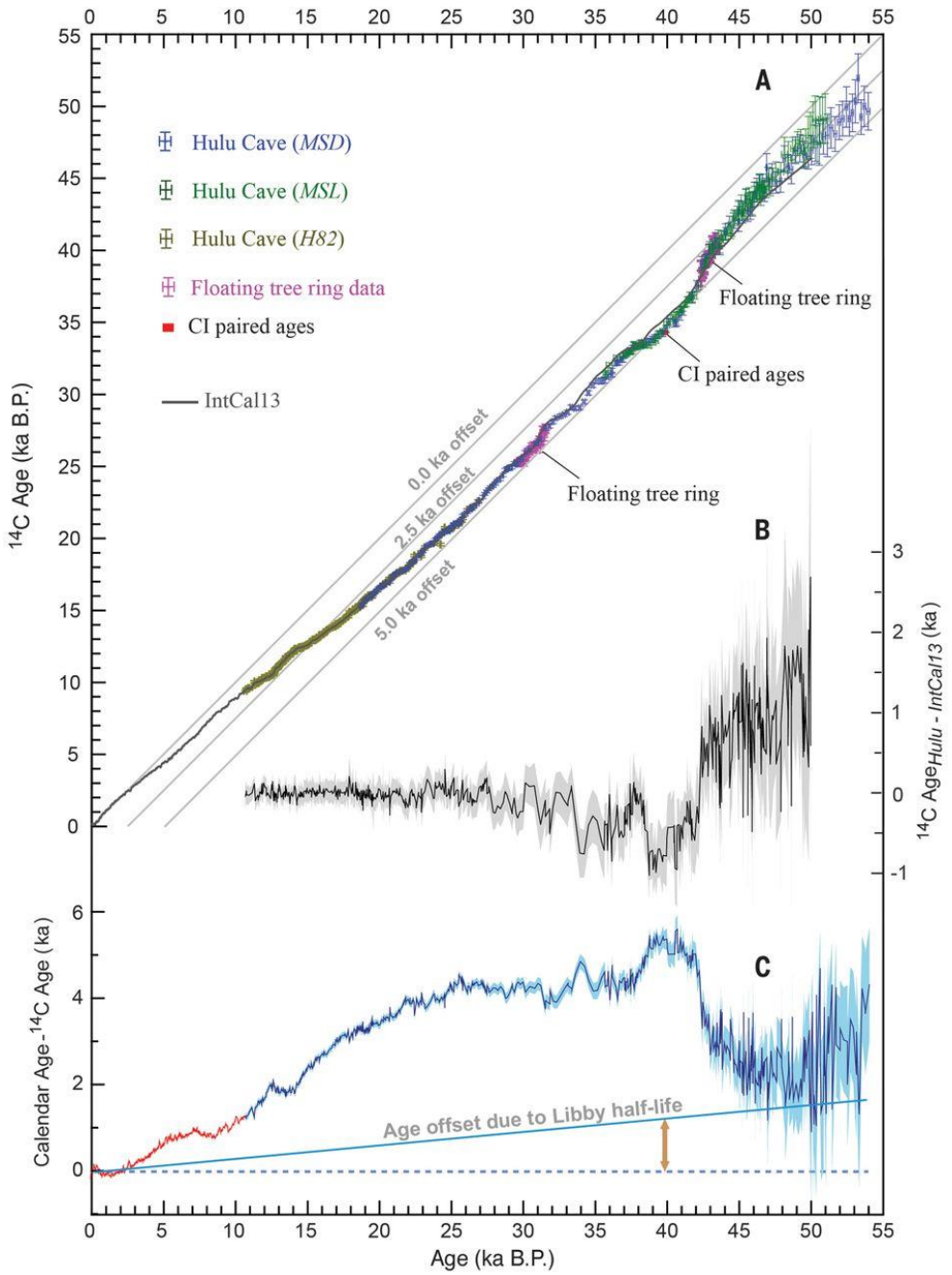

Figure 1. Hulu speleothem ^{14}C versus ^{230}Th ages and comparison between Hulu and IntCal13 ^{14}C ages. (A) Hulu [olive-brown, H82 (*8*); blue, MSD, and green, MSL (this study), and IntCal13 ^{14}C (*17*)] vs. ^{230}Th ages. ^{14}C error bars are 1σ. For clarity, uncertainties in IntCal13 are not shown. The floating tree ring $\Delta^{14}C$ datasets (purple) (*14*, *15*) are tuned to the Hulu ^{14}C record (*11*). The red square (1σ) is the independent data point based on ^{14}C measurements on wood associated with the Ar-Ar dated Campanian Ignimbrite (*13*). (**B**) ^{14}C age difference (black) between Hulu dataset and IntCal13 (*17*). The gray envelope shows the uncertainty (1σ). Hulu ^{14}C ages are corrected for the DCF (450 ± 70 years) (*8*). (**C**) Calendar age minus IntCal13 (red)/Hulu (blue) ^{14}C age. The light blue envelope shows the uncertainty (1σ). The three Hulu sample datasets replicate over contemporary growth periods. Hulu Cave ^{14}C data are consistent with IntCal13 between ~10.6 and 33.3 ka B.P. but lower in ^{14}C ages between ~33.3 and 42 ka B.P. and higher between 42 and 53 ka B.P.

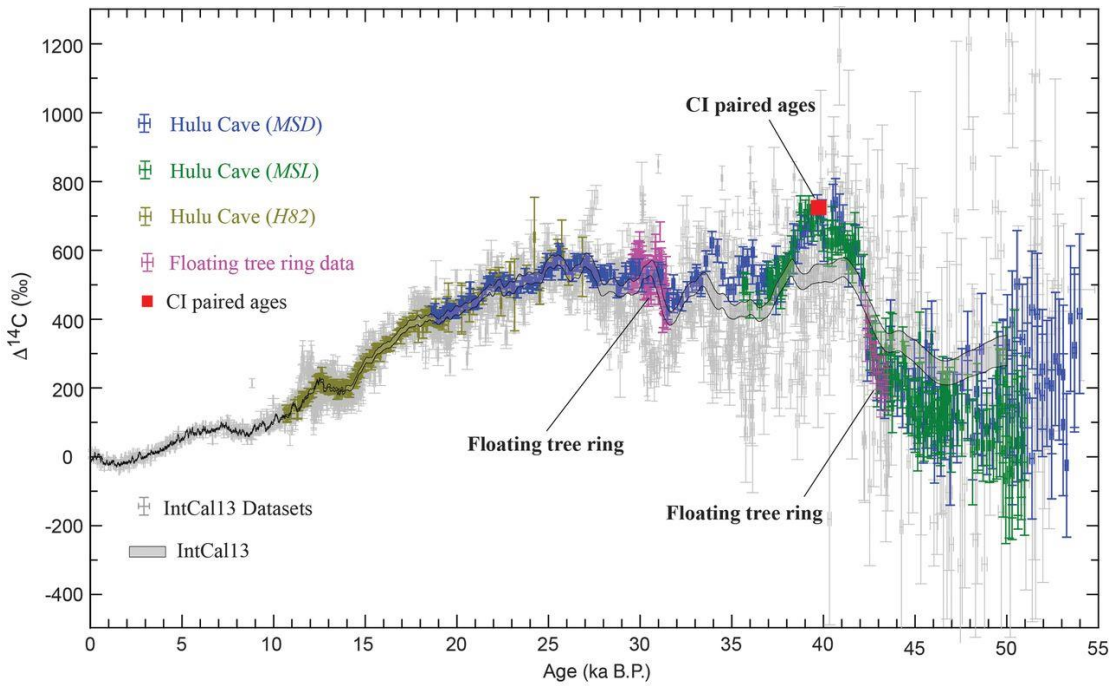

Figure 2. Comparison of Hulu $\Delta^{14}C$ data with IntCal13. Hulu $\Delta^{14}C$ data are shown with error bars with the same color codes as in Fig. 1. IntCal13 and its dataset (*17*) are shown in the gray envelope and gray bars. ^{14}C error bars are 1σ. Hulu data overlap with IntCal13 between ~10.6 and 33.3 ka B.P.; however, there are substantial offsets, particularly before 30 ka B.P., and the Hulu record exhibits substantial previously unknown millennial-scale structure. The purple error bars and red square are the floating tree ring series and Campanian Ignimbrite data, as in Fig. 1.